The University Of Sheffield.

Quantum Cascade lasers in the Mid-infrared

Xintao Chen

A thesis submitted for the degree of Master of Philosophy

Department of Electronic and Electrical Engineering

The University of Sheffield

Acknowledgement

I would like to express my deep appreciation to my supervisor Prof Jon Heffernan and Dr Ian Farrer for their valuable guidance and suggestions on my project during the last two years. I would also like to appreciate the help and guidance offered by Tim Roberts during my study and experimental work. Finally, I wish to thank my parents and friends for supporting me throughout my study.

Contents

Abstract 3
Chapter 1 Introduction 4
Chapter 2 Literature Review 5
2.1 Quantum well 5
2.2 Quantum cascade laser (QCL) 5
2.3 Interband cascade laser (ICL) 7
2.4 Example of different designs on cascade lasers 9
Chapter 3 Simulation of simple ICLs and QCLs 15
3.1 Relationship between emission wavelength and well width 15
3.2 Electron distribution analysis 18
3.3 Simulation of Quantum Cascade Lasers (QCLs) 20
3.3.1 Wannier-Stark levels 22
3.3.2 Gain characteristics 23
3.3.3 IV characteristics 25
Chapter 4 Experiments on broad area and narrow ridge lasers 27
4.1 Fabrication and testing of a broad area QDLs 27
4.2 Characterisation of QDL 32
4.3 Reproducibility 36
4.4 Fabrication and characterization of Narrow ridge QCLs 39
4.5 Results 45
4.5.1 Power-Current (L-I) characterisation 46
4.5.2 Spectra analysis 51
4.5.3 Calculation of the internal loss in the laser cavity 53
High Reflective (HR) coated QCL 54
4.6 Summary and conclusion 56
Chapter 5 Conclusions and Future recommendation 58
Challenges and future recommendations 59
Appendix 61
References 67

Abstract

Cascade lasers includes quantum cascade lasers (QCLs) and interband cascade lasers (ICLs). QCL and ICL have similar structures and working principles. A common feature of these two kinds of cascade lasers is electron recycling, which means that one electron can produce multiple photons. This greatly improves the efficiency of the devices at these wavelengths, because it is difficult to find good narrow gap materials which would allow lasing at this wavelength. Therefore, cascade effect can mitigate this problem. In addition, Mid-infrared (MIR) light sources is in great demand because this region contains absorption features of many important molecules, and therefore, can provide a variety of applications.

It is important to investigate and evaluate the performance of current state-of-art devices, and it is worth exploring the way to improve the performance of devices. This can make the applications more competitive in the market and can help to increase the efficiency. This thesis will talk about some simulations of QCLs and ICLs and will focus on the discussion on experimental results for fabricated structures.

In this project, we investigated the use of nextnano to simulate previously designed QCLs as well as some initial attempt on ICLs. QCLs with different number of periods were then fabricated and tested experimentally to explore the effect of increasing the number of active regions in the structure. We found a reduced threshold current density in the device fabricated from MR 3881 (42 periods) compared with MR 3877 (35 periods), and the reduction in threshold current density matched up with the increase of gain. The calculation of internal loss was also carried out and compared with literature. Moreover, the testing of highly-reflective (HR) coated devices for MR3877 were also attempted by evaporating an amount of MgF_2 and a reduction in threshold current was obtained.

Chapter 1 Introduction

Quantum cascade lasers (QCLs) and interband cascade lasers (ICLs) are considered as promising light sources for many applications like chemical sensing, pollution monitoring and free-space communications as well as some medical applications in the mid-infrared. Therefore, the investigation of these two types of cascade lasers is of great interest. This project will concentrate on the study of quantum cascade lasers. The aim of this project is to fabricate a previously designed QCL and test the performance of the fabricated lasers. To achieve this, initial training on fabricating broad area lasers would be necessary. Simulation is also necessary to help us understand the performance of our lasers. Besides, some novel ideas on ICL would be studied to provide a fresh knowledge about current-state-of-art cascade devices.

There are many factors/parameters which are closely related to the performance of QCLs such as number of periods, layer composition, doping concentration, internal loss etc. It is important to understand how these factors affect the performance of QCLs. As the number of periods of the active region of a QCL increases, the threshold current density is expected to reduce as higher gain is obtained. However, a QCL device might be degraded once a critical number of periods is reached. Therefore, the aim of this work was to explore the effect of number of periods on the performance of QCLs. Secondly, since the internal loss of fabricated devices is a critical aspect of laser operation, the internal loss was calculated and compared with current-state-of-art QCLs in order to confirm the quality of epitaxial growth and fabrication. Thirdly, the effect of HR coatings was investigated to improve the performance of the devices and confirm that the laser threshold was primarily determined by gain and optical loss only. To achieve this, QCL devices made from two different wafers with different number of periods (35 and 42) are fabricated.

This report will discuss on the basic concept and working principles of both QCLs and ICLs, and demonstrate some simulations run with Nextnano ++ on ICLs. The details of these two type of cascade lasers will be discussed in the literature review. However, the literature review will focus more on ICLs which are a less developed structure.

Despite the fact that the simulation of ICL is still very limited at the moment, only the band structures and carrier distributions can be modelled under a given electric field. Finally, some future recommendations will be briefly discussed.

Chapter 2 Literature Review

2.1 Quantum well

A quantum well is usually defined as a thin layer of a semiconductor material of narrow bandgap sandwiched between semiconductor layers of wider bandgap. The well and barrier are in energy space. It is a particular type of heterostructure in which the "well" layer is very thin and embedded in two "barrier" layers. Both electrons and holes can be confined in the quantum well. The energy levels in a quantum well are quantised and discrete, and can be engineered by varying the thickness and composition of the well layer. As the properties are very sensitive to the well thickness, it is necessary to use modern epitaxial growth techniques of high degree precision such as Molecular Beam Epitaxy (MBE) or Metalorganic vapour phase epitaxy (MOVCD) [1-3]. The energy states can be further modified by strain, which is caused by lattice mismatch between two materials.

In a traditional diode laser using multiple quantum wells, the transitions are in the form of interband recombination of electrons and holes between the conduction and valence band. The essential conditions to achieve lasing are: population inversion, gain and feedback. Population inversion means that the population of active carriers in upper state should always be higher than the lower state, in order to obtain a positive optical gain. [4-5] This can usually be achieved electrically by current injection because under thermal equilibrium the population in lower state is normally higher than that in upper state.

2.2 Quantum cascade laser (QCL)

A QCL is a unipolar device, in which the photon is emitted by intraband transition, which happens between quantised subband energy level within the same band (normally conduction band), [5] as shown in Fig 2.2.1. This means only one type of carrier (normally electrons) is involved.

The core idea of the QCL was first proposed by Kazarinov and Suris in 1971 [2], which is to employ inter-subband transitions to achieve radiation amplification. This idea was realised at Bell Laboratories in 1994 [6], following the development of growth techniques such as MBE or MOVCD that provide accurate control of layer thickness down to single atomic monolayer level. [1]

The spectral tuning range of QCLs is in the Mid-infrared (MIR) covering from ~3-25 µm [1,7]. The most important feature of the QCL is that the emission wavelength has potential for large

tuning range by tailoring the quantum well thickness without being limited by the bandgap of material. [1,5,7] This is as opposed to conventional diode laser which strongly depends on the material itself. The shortest emission wavelength is limited by conduction band offset, which allows the operation in the mid-infra red where interband materials have limited availability.

In recent two decades since the QCL was invented, remarkable performance levels have been achieved for QCLs operating in the mid-Infrared. In particular, emitted powers up to 5 W in continuous wave (CW) operation at room temperature with wall-plug efficiency up to 21% (27% in pulsed mode have been achieved. [8-12]

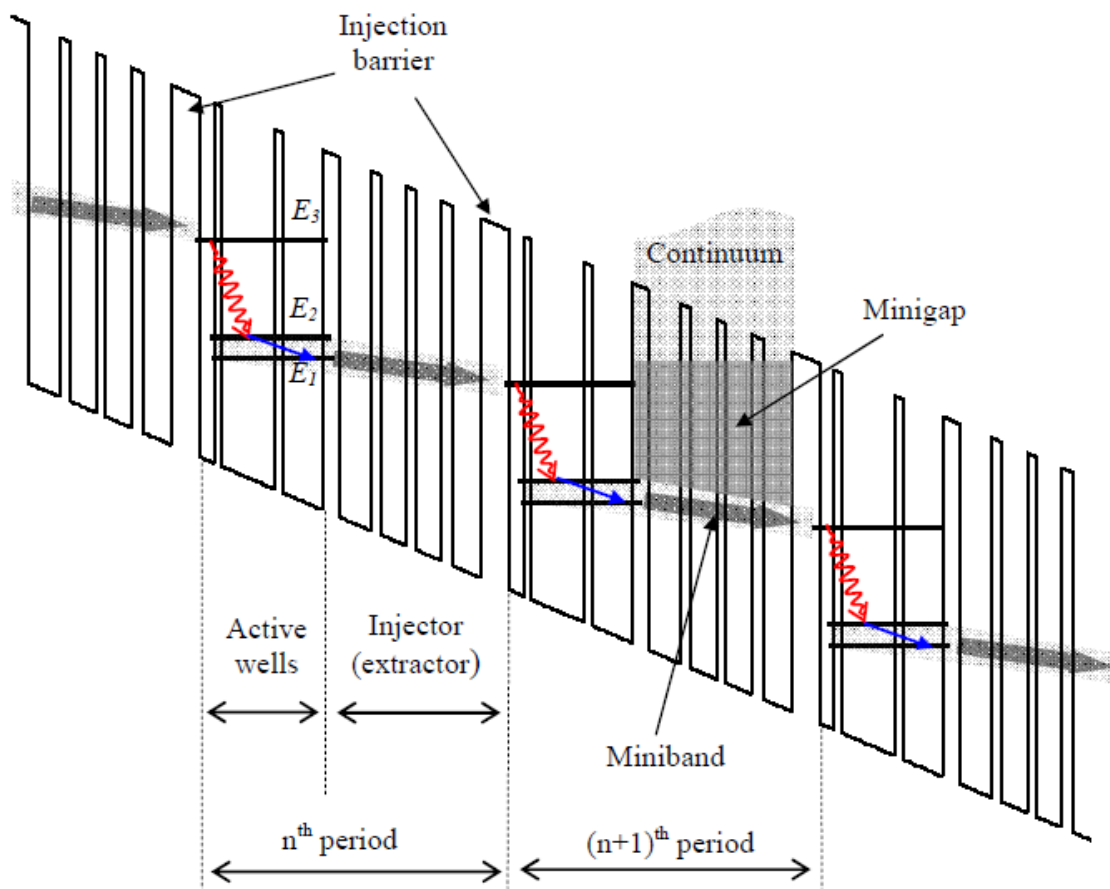

Fig 2.2.1 Schematic diagram of a typical QCL cascades region [13]

Fig 2.2.1 shows the band profile of active layers for a typical QCL. The active layers consist of a number of repeated periods (normally 20-100) [5]. Each period is composed of an active region where the photon is emitted by optical transition, and an electron injector. Both the active wells and injectors are composed of multiple quantum wells and barriers or a superlattice

[5]. Under a certain bias, the electron injector is lined up with the excited state in the next active well. Thus, the electrons are injected to the excited state in the next active region through resonant tunnelling. This feature allows electron recycling, meaning that one injected electron can produce multiple photons and travel through the whole structure. The number of photons that can be produced during the whole process depends on the number of stages. [1]

The population inversion in a QCL is achieved by appropriate engineering of electron lifetime at different stages. As shown in Fig 2.2.1, the radiative recombination is between the second excited state (E3) and first excited state (E2). The relaxation time τ_{32} is relatively long compared with τ_{21} and the time that the electrons escape from the ground state (E1) to the excited state of next period. Due to very fast resonant tunnelling, the number of electrons in E2 is always less than that in E3, this is how a population inversion achieved in a three-well system. [5]

2.3 Interband cascade laser (ICL)

The interband cascade laser (ICL) is different from any other type of semiconductor lasers. The ICL is a combination of traditional diode laser and quantum cascade laser (QCL). It is a bipolar device, in which the optical transitions involve both electrons and holes. [14] The cascade mechanism is also employed in ICLs, which again can provide carrier recycling, making the device much more efficient compared with normal laser diode. Due to less cascade stages in the active layers, an ICL can have lower operating voltage than a QCL, which makes it useful for applications requiring low voltage or electrical power. For example, people have investigated on using them for sensing systems on spacecraft.

Current-state-of-art GaSb-based ICLs can normally cover 3-6um spectral window with room temperature (RT) continuous wave performance. The longest wavelength achieved to date, is up to 11.2 μm with highest operating temperature of 130K by using InAs substrate and replacing the cladding layer with n^+ InAs plasmon waveguide. [15]

The ICL was first invented in 1994 by Ruiqing Yang [16], in which the single type-II alignment in the active well was replaced by a "W" configuration which incorporate an InAs electron quantum well on each side of the GaInSb hole quantum well. [17] In an ICL, the carriers are produced internally, where the holes are injected to the active region through a hole injector in the valence band, and the electrons are injected through electon injectors in the conduction band. The "W" structure is regarded as a standard configuration for current devices although

the overlap between hole and electron wavefunctions decreases, the gain is increased in this case. [14]

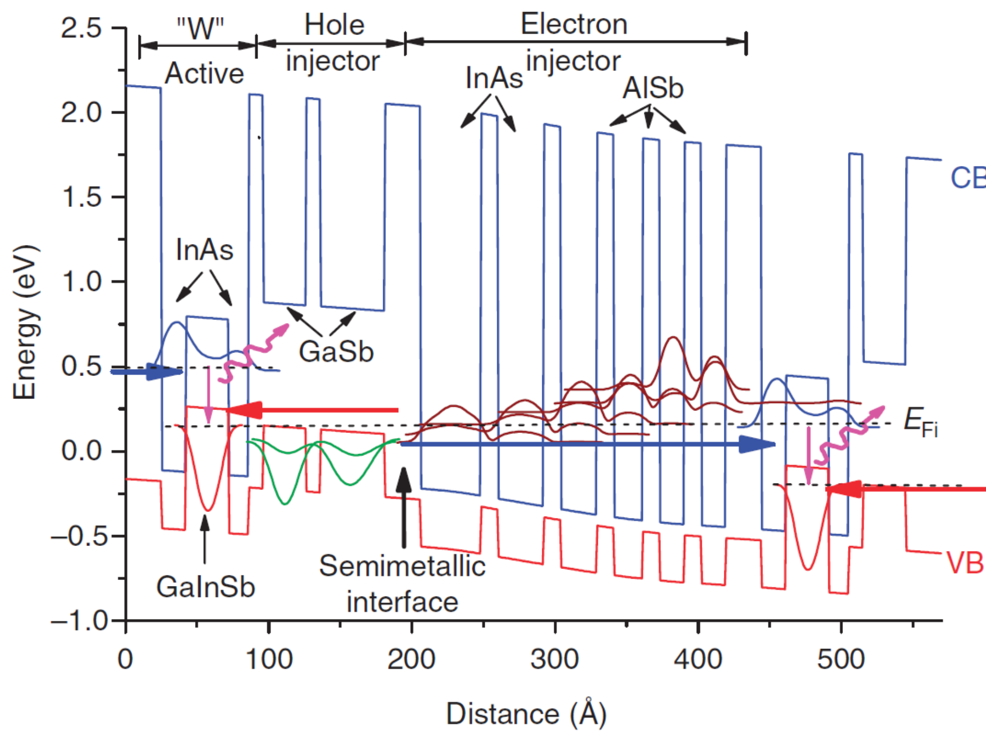

Fig 2.3.1 Schematic band diagram of 1.5 periods of an ICL [14]

As shown in Fig 2.3.1 (taken from reference 14), the active core of an ICL consists of a number of repeated stages, each stage is formed by the active quantum wells, the hole injector, and the electron injector. The active region can either have a type II or type I alignment. The semi-metallic interface acts as a barrier, to isolate the hole injector that is comprised of GaSb/AlSb quantum wells, with the electron injector consisting of InAs/AlSb quantum wells. [14]

In a conventional multiple quantum well diode laser, in which electrons and holes are injected into the active well from two sides of a p-n junction the threshold current density is given by MJ, while J is the current density of a single well, M is the number of quantum wells. However, in an ICL, the cascade mechanism can mitigate this issue by connecting those quantum wells in series. Thus, the same electron can flow through the whole structure and produce multiple photonsJJ, the threshold power density is then reduced without introducing much additional voltage or current. [18]

Vurgaftman *et al.* shows that for those devices with moderately doped electron injectors, the electrons reside mostly in the injector whilst most of the holes transfers to the active region. This lead to a large contrast of the electron and hole population. [19] Heavily doped InAs

quantum wells in the electron injector was then proposed by this group to rebalance the carriers in the active region, which significantly improved the performance of ICLs in terms of threshold current density. After rebalancing of carriers, the number of electrons and holes in the active region become much more comparable.

2.4 Example of different designs on cascade lasers

Ruiqing Yang's group has made impressive progress on InAs-based ICLs. The emission wavelength of an ICL was extended up to 11 μm by using InAs substrate. [15] They introduced that the cladding layers for long-wavelength ICLs would be thicker, which introduce extra loss and complicate the growth process. [15] In order to reduce the thickness of the cladding later and supress the optical loss, InAs plasmon layers are introduced to replace the super lattice (SL) layers due to the lower refractive index and the higher thermal conductivity. [15] This enables room temperature operation beyond 6 μm as wells as lasing at even longer wavelength. [20, 21]

In order to further decrease the waveguide loss, a hybrid waveguide consisting of metal and dielectric layers was employed to replace the regular top cladding layer. [22] The performance of the structure with regular top cladding layer and the one with hybrid cladding layer were compared in this paper.

They reported that a 15-μm-wide and 1.25-mm-long device near 5.27 μm up to 247 K under CW operation, and 5.3 μm up to 295 K in pulsed mode. Their results show that the maximum operating temperature in CW mode is higher than previously reported devices with SL cladding layers at similar wavelengths, [23, 24] which agrees with the assumption that plasmon waveguide have an improved heat dissipation.

They concluded that the defect-related Shockley-Read-Hall recombination dominating at low temperatures leads to more significant differences at low temperatures. They also suggested that similar defects has been observed for previous ICLs [25] and type-II SL detectors especially for Sb-based devices due to the non-uniform nature of materials and the processing variation.

The following paper introduces InAs-based single-mode emission ICLs by Distributed Feedback (DFB) structure. [26] The following equation is used to determine the DFB grating period Λ:

$$\lambda = 2\Lambda N_{eff} \qquad (1) \qquad [26]$$

where λ is the emission wavelength and N_{eff} is the effective index of the waveguide.

In this work, the structure here is similar to that discussed in previous paper, without a conventional top cladding layer. The waveguide core was formed by the 8 cascade stages with undoped n-type InAs separate confinement layers (SCLs) on both sides. This waveguide core was in turn, sandwiched between a thick n^+ InAs bottom cladding an n^+ InAs top contact layers. Besides, a transition layer was inserted between the SCLs and the bottom cladding , as well as the top contact layers. Apart from this, they suggested that the device performance can be further improved when a top dielectric layer is inserted to form a hybrid waveguide [22], as discussed previously.

Their simulation results indicates that the effective index of this structure is approximately 3.4 and the designed grating period calculated from equation (1) is 655 nm.

They reported that a current tuning rate of 16 nm/A near 4.49 µm was observed at 160 K, and a tuning range of 2 nm when current was increased from 140 to 260 mA. The SMSR in this case was about 30 dB. They observed the DFB mode emission from 150 to 180 K and the laser started lasing at FP mode above 185 K.

They also found that the devices lasing at DFB mode had higher threshold current density than the FP lasers. Nevertheless, a laser with DFB grating without lasing at the DFB mode showed a similar performance as the FP laser, leading to the conclusion that the metal grating itself might not affect the laser performance too much.

It is also suggested that the wide mesa may allow multiple lateral modes to coexist along the mesa perpendicular to the longitudinal direction [27-29], a single fundamental lateral mode can be achieved by using a narrow ridge [30] or introducing additional loss to the higher-order modes [31].

The next two papers of Yang’s group are based on the tunability of an ICL and dual-wavelength emission [32,33]. In 2012, Li *et al.* proposed a dual-wavelength structure by stacking two cascade stages with different emission wavelengths together. [32] The bottom cascade region is composed of 12 identical stages and designed to lase at the longer wavelength (LW) near 6 µm. The top cascade region has 9 cascade stages and lase at the shorter wavelength (SW) near 5 µm.

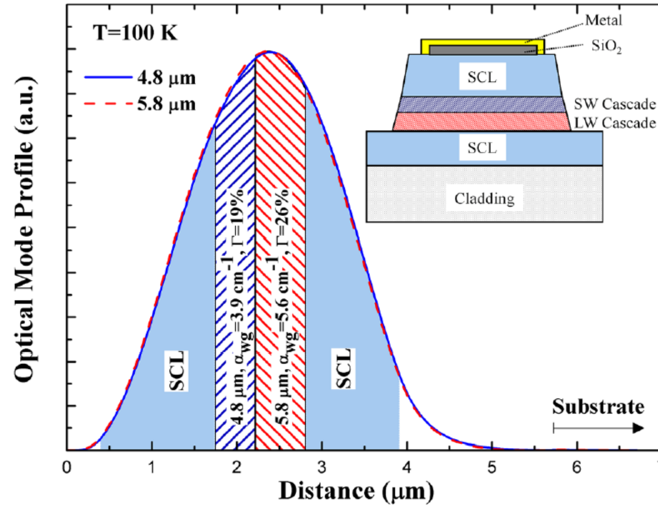

Fig 2.3.2 Layer composition and optical mode profile of the single waveguide dual-wavelength structure. [32]

As shown in Fig 2.3.2 (taken from reference 32) that two cascade regions sandwiched by bottom and top undoped InAs SCLs. A highly doped n^{++}-type bottom cladding layer is underneath the bottom SCL and a n^{++}-type InAs contact layer is above the top SCL.

Some 150-μm-wide deep-etched broad area lasers were processed by contact photolithography and wet etching. A dielectric layer was then deposited in the middle of the laser bars, following with the deposition of metal contact on the top centre of the laser bars. They suggested a reduced optical loss for this kind of hybrid waveguide. [22]

Their experimental results indicate that only the LW region was able to lase in CW operation. They suggested that the SW region contributed to the high threshold voltage in CW mode. Besides, their results show that the gain peak jumped from 6.2 μm to 5.2 μm above 220 K in pulsed mode, indicating that it started lasing from SW region. The dual-wavelength emission could thus be achieved below 220 K at certain current levels.

Their simulations show that the confinement factor is larger in LW region while the waveguide loss is smaller for SW region. Therefore, the threshold of both sectors is considered to be about the same combing the above two factors. Thus, they attributed the high threshold current of SW region to its high absorption loss, because the energy of the emitted photon in the SW region is larger than the band gap of the LW region, meaning that the emitted photon from the SW region could potentially be absorbed by the LW region.

Regarding the tunability of ICLs, Jiang *et al.* from the same group has demonstrated an electrically widely tunable device in 2014. They suggested a way to combine the Stark effect and the heating effect, both of which can contribute to significant red-shift.

Stark effect indicates how the energy of an interband transition (ΔE) change with the electric field (F), the equation which describes the Stark shift can be written as [33]:

$$\Delta E = -q|\Delta F|(z_e - z_h) \qquad (2)$$

where q represents the electron charge and ΔF is the change of the electric field, (z_e-z_h) is the interband dipole of the electron and hole distribution. Whether the value of the interband dipole is negative or positive determines the blue-shift or red-shift of the emission wavelength with an increase of the electric field. Thus the electron distribution is mainly in the left or right InAs quantum well matters. Some work in the past shows that when the electron distribution was designed mainly in the left side of the active region, blue-shift occurred with the increase of electric field. [34,35] However, the electron distribution can move from left to right when increasing the electron field, as shown in Fig 2.3.3.

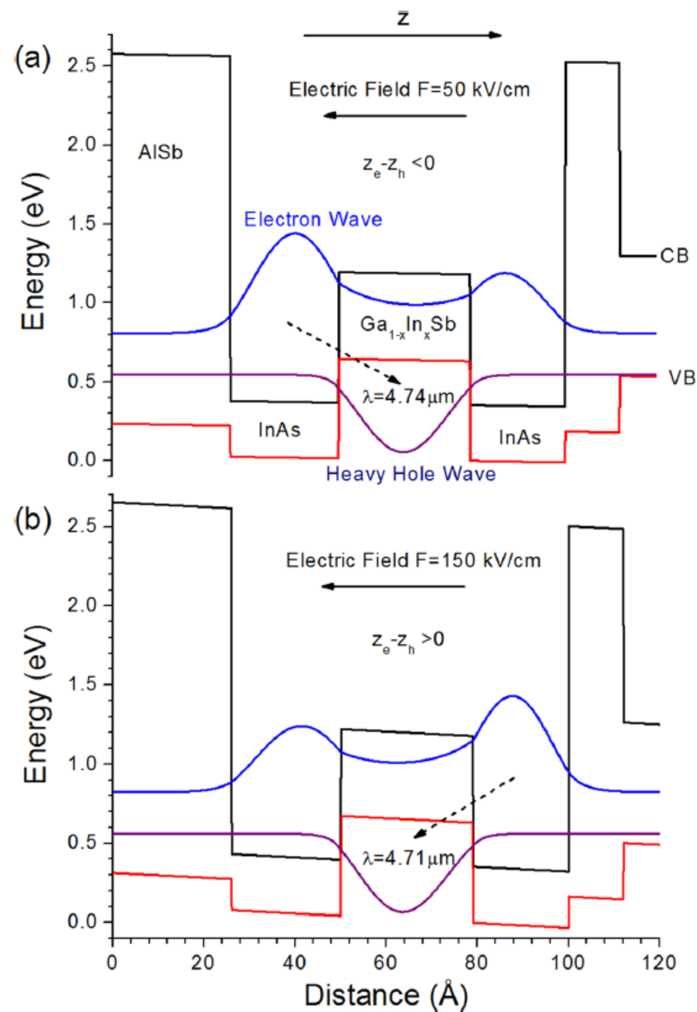

Fig 2.3.7 Electron and hole distribution in the active region at various electric field. [32]

They observed very similar threshold current density to the value of other devices from the same wafer but had a slightly higher voltage compared to typical values. Jiang *et al.* suggested that this higher voltage may result in a larger electric field across the structure, which pushed the electron distribution to the right side. Therefore, a red-shift was caused when increasing the bias.

They suggested that a lower tuning rate was observed for shallow-etched devices , meaning that the deep-etched devices have stronger heating effect. In order to examine the Stark effect described by equation (1), devices made from other wafers were then only shallow etched to reduce the heating effect.

Their results exhibited that Stark effect alone cannot lead to above-threshold wavelength shift. The large tuning range and rate should be achieved by the combination of the Stark effect and heating effect.

After the experiments based on these four wafers, they attempted a new structure which comprises of three InAs quantum wells in the active regions, the structure with multiple coupled quantum wells has been proved to have a stronger Stark effect compared with a single quantum well. [36, 37]

In conclusion, QCL is a unipolar device which is composed of a number of repeated periods of active regions and electron injectors. During the past 20 years, there has been much progress on QCL. The emission wavelength of this kind of device covers from 3 to 25 μm by engineering the layer thickness rather than the bandgap of materials. The cascade regime is used to achieve electron recycling, which makes it an efficient device. Thus, the effect of the number of periods on the performance of QCL is of great interest. In our project, we fabricated devices with 35 and 42 periods for comparison. We also attempted to calculate the internal loss of our device and compare with current-state-of-art QCLs in order to confirm the quality of epitaxial growth and fabrication. To improve the performance of our devices, the effect of HR coatings was also investigated by covering the back facet of our devices with MgF_2.

There has also been much progress in the last 20 years on ICL with the device performance that already demonstrated. Current issues in performance of ICLs are the coverage of wavelengths, high threshold for long wavelength devices etc. Therefore, areas of research focus on the extension of wavelength to shorter or longer and being able to lase at a lower threshold current and even at room temperature. One of the issues and the one is the subject of this thesis is to explore the tunability of ICLs by engineering the emission wavelength using Stark effect, which will be discussed in the next chapter. Moreover, multiple-wavelength ICLs can be inspired from the dual-wavelength devices mentioned in the literature, which allows the device to lase at multiple wavelengths.

Chapter 3 Simulation of simple ICLs and QCLs

Our simulations on ICLs have been run with Nextnano. Simulation of ICL is a new module in this software, and hence the simulation is still rather limited at the moment but has been used to provide fresh insight. Single band **k · p** model was used for the simulation of ICL in nextnano, this means that only one band is considered in the simulation. Only the band structure can be obtained from the simulation, and the Schrodinger Equation can be solved under a given electric field. Therefore, we are able to simulate the transition energy between the electron level and the hole level based on different structures from literature. Hence, we were able to calculate the emission wavelength and investigate the relationship between the emission wavelength and the width of InAs quantum well in the active region, which is an important aspect of the laser design and its sensitivity to design parameters and epitaxy capability. In addition, we were able to simulate some "three quantum well" structures mentioned in Chapter 2. Hence, the Stark effect could be investigated, which is important because we will be able to know how the electron distribution varies with InAs well width.

Simulation of QCL is a mature module of Nextnano compared with that of ICL. The code of Nextnano.QCL is based on the non-equilibrium Green's functions (NEGF) which allows the consideration of quantum transport effects and scattering mechanisms.

The calculation starts from solving the single-band effective mass Schrodinger Equation in real space to obtain the minibands in the structure. The scattering terms are then calculated for the consideration of optical phonons, acoustic phonons, interface roughness and electron-electron scatterings etc. Then, the NEGF solver will calculate the scattering processes and the Green's functions in a self-consistent way which starts from an initial guess of Green's functions. The Green's functions are calculated within a number of iterations until the convergence is reached. In the meantime, the Poisson's equation is also calculated self-consistently to get the mean-field electrostatic potential. The solutions will give us the current density and carrier density. The gain spectrum will also be calculated if specified in the input file.

3.1 Relationship between emission wavelength and well width

In order to investigate the relationship between the emission wavelength and the InAs well thickness in the active region, the structures with different well thickness was simulated. These structures come from three different papers, as shown in table 3.1.1. The thickness of InAs quantum well is gradually increased. From the simulations, we will also be able to find out that

whether the fluctuations InAs well thickness that may arise from the epitaxy process has significant effects on the emission wavelength.

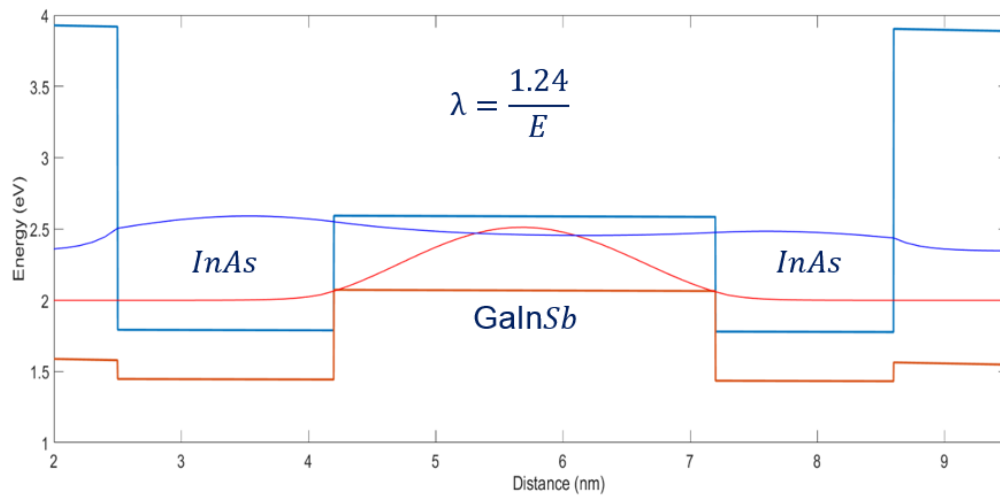

Fig 3.1.1 Simulated active region of an ICL formed of InAs/GaInSb/InAs quantum wells and the wavefunctions in the conduction band (blue line) and the valence band (red line).

The simulation is run by Nextnano, in which the software can calculate the Schodinger Equation under a given electric field. The band structure and energy levels will be calculated. The result can provide the information on wave functions and the possibility of finding electrons at a certain position.

Fig3.1.1 shows the active region of an ICL taken from [19], which is composed of InAs/GaInSb/InAs quantum wells. The wavefunctions in the conduction band and valence band are shown in blue line and red line respectively, which is calculated through Schrodinger Equation. By varying the width of the quantum wells or the composition of the GaInSb barrier, the energy level in the wells will shift upwards or downwards, hence the emission wavelength will be changed. The thickness of the layers in the injectors also need to be adjusted properly to line up the energy levels in the injectors with that in the active region.

Table 3.1.1 Comparison of the emission wavelength between the simulated results and reported value

$InAs$	$Ga_{0.65}In_{0.35}Sb$	$InAs$	Reported Wavelength	Simulated Result
14 nm	30 nm	11 nm	2.8 μm [38]	2.98 μm
17 nm	30 nm	14 nm	3.6 μm [19]	3.59 μm
22 nm	29 nm	20 nm	4.6 μm [39]	4.75 μm

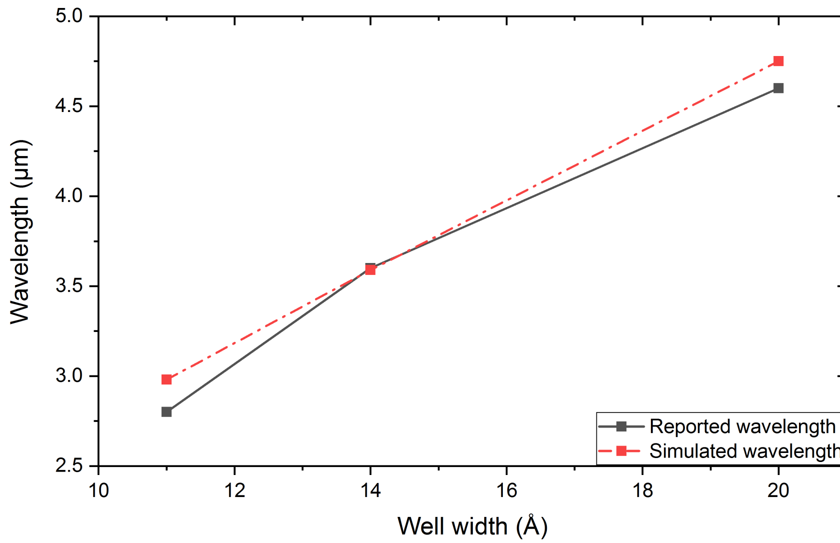

Fig 3.1.2 Relationship between the emission wavelength (solid line: reported value, dot line: simulated value) and the InAs layer thickness

Table 3.1.1 shows that the emission wavelength increases with the increase of InAs well width. The simulated result can agree very well with the reported value. The simulations are based on single band $\mathbf{k} \cdot \mathbf{p}$ model. Further improvements on 6 band and 8 band $\mathbf{k} \cdot \mathbf{p}$ model are expected in future work, due to the interaction between more bands will be considered.

Fig 3.1.2 demonstrates the relationship between the simulated value and the InAs layer thickness, while there is a slightly offset between the reported lasing wavelength in the literature and our simulated value. More data points is required to explore whether the relationship is truly linear. The trend of the reported results and simulated results are the same whilst the transition energies are not exactly matched up. However, this error is acceptable and it is reasonable because the laser is working on the balance of gain and loss, whilst the calculations here are only showing transition energies under the bias condition of lasing. Besides, as mentioned above, single band $\mathbf{k} \cdot \mathbf{p}$ model does not include consideration of the interaction of different bands, which can also lead to the difference of our simulated results and the actual lasing wavelength reported in the literature. Apart from that, other factors which may affect the emission wavelength are also not able to be considered at this point, such as scattering, strain etc. The author of ICL simulation file might use slightly different parameters with others. Apart from the reason from simulation itself, it is also possible that the actual lasing wavelength reported in literature is not accurate due to the variation during the device fabrication. Therefore, it is important to conduct more tests to examine the relationship between the simulated

wavelength and experimental lasing wavelength, to get a good control of wavelength for future design.

3.2 Electron distribution analysis

As mentioned in Chapter 2, it is important to look at the electron distribution in the active region if the Stark effect is of interest. The electron distribution can be engineered by controlling the quantum wells in the structure. It is necessary to have a good control of electron distribution because this is related to the actual transition in the wells and thus, it will affect the emission wavelength. Besides, it will also be helpful to guide how to explore the tunability of a laser by varying the electron distribution. The structures in Ref [33] have been modelled to observe whether the electron wave function is mainly in the left or right InAs quantum well.

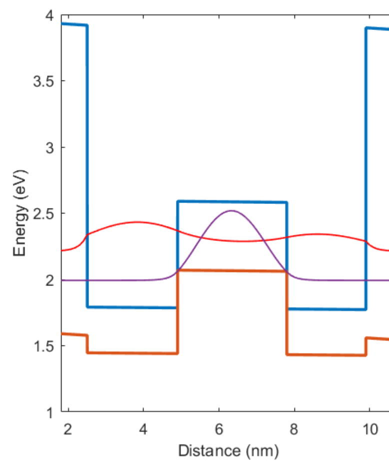

(a)

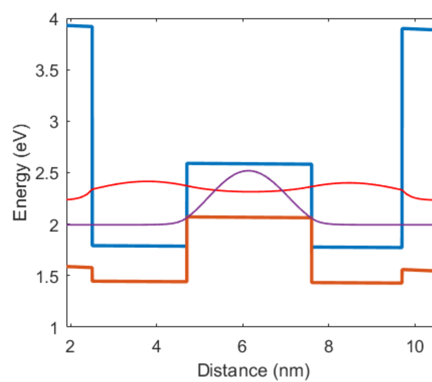

(b)

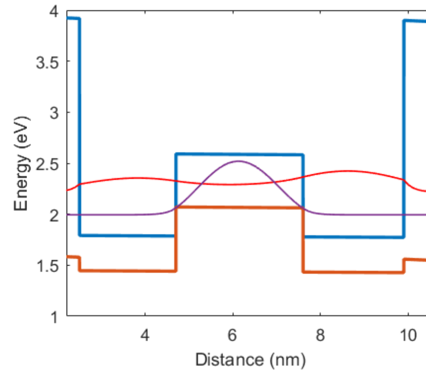

(c)

Fig 3.2.1 The electron distributions at various InAs/GaInSb/InAs layer thickness (a)24/29/21 (b) 22/29/21 (c) 22/29/23 nm

Fig 3.2.1 shows the electron distributions in the active region at different layer thickness. The red lines show the wave functions in the conduction band and the purple lines show the wavefunctions in the valence band. The wavefunctions are solved through Schrodinger Equation and represents the possibility of finding electrons in a specified position. Therefore, this property can be used for the future design of tunable devices. For example, we can model the wavefunctions of a structure and look for our target wavelength for our real devices. As the thickness of the left InAs quantum well decreases and that of the right InAs layer increases, the electron distribution starts to move from the left side to right side. This verifies the statements in the literature [33] that different thicknesses for the InAs quantum wells would result in variations of electron distributions.

The "three quantum well" structure (Fig 3.2.2) suggested by Jiang *et al.* [4] was also modelled, because multiple coupled quantum wells in the active region has been proved to have a stronger Stark effect.

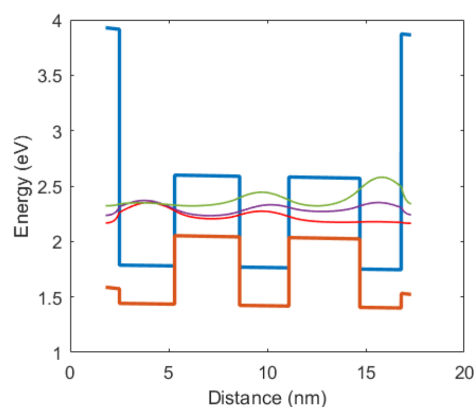

Fig 3.2.2 The schematic diagram of the "three quantum well" structure with the wave functions at various electric field

In order to investigate the electron distribution in a better way, a three-well system was simulated by Nextnano. There were no reports of simulation of this type of structure in the literature therefore the structure was investigated in this thesis using Nextnano. It was expected that the electron wave function will shift from the left side to the right side with the increase of electric field. As can be seen in Fig 3.2.2, the electron mainly sit in the first well (red line) at beginning, it then starts moving to the middle well when increasing the electric field (purple line). Finally, the electrons move to the third well when further increasing the electric field. The simulation of this structure under different electric field verifies this statement is true. Hence, this work supports the explanations given in the literature and this is helpful to understand why such structure with multiple quantum wells can have a stronger Stark effect.

To sum up, the effect of well width on emission wavelength and the electron distribution analysis were covered in this section. These studies could contribute to future designs about tunnable devices by controlling the position of electrons and hence, the actual transition, which will affect the lasing wavelength.

3.3 Simulation of Quantum Cascade Lasers (QCLs)

In order to establish a better understanding on the performance of the QCL, and to investigate the IV and gain characteristics of a previously designed QCL emitting at 5.7 μm, the QCL structure designed to emit at this wavelength have been simulated by nextnano.QCL. It is a module provided by nextnano software specifically for QCL. The software can provide a general idea on the properties of different materials. It can give us a better calculation based on quantum mechanisms and consideration of doping and different scattering mechanisms, which are not included in ICL module yet. As nextnano.QCL is relatively a mature module, we were be able to compare the simulation with our experimental results. The results can be used to compare the performance of different materials and evaluate the influence when parameters are changed. In addition, enough knowledge on the simulation of QCL can help to improve the performance of devices by optimising the structures.

In the software, different scattering mechanisms are taken into consideration (LO phonon, interface roughness etc.). Non-equilibrium Green's Function model is used in the Nextnano software. There is a feedback loop that the Green's function and Poisson equation was calculated self consistently to improve the accuracy of the results. The calculation is very huge

and typically take more than 20 hours, because the iterations will only complete once the Green's function and Poisson function converges. From the simulation, the Wannier-Stark energy levels, I-V characteristics, density of states, gain and some important information can be obtained.

The structure simulated is an InP based InGaAs/AlInAs QCLs. Each period of the active region is composed of a superlattice of $In_{(0.6)}Ga_{(0.4)}As/Al_{(0.58)}In_{(0.42)}As$. Table 3.3.1 shows the structure of our simulated device. This simulation is compared with experimental work in the next chapter. The structure is designed for 5-6μm lasing, and used to investigate the effect of number of periods on the threshold current density.

Table 3.3.1 The structure details of our simulation

Thickness	**Material**	**doping**	**repeats**	**In fraction**	
31 Å	InGaAs		35	0.6	
18 Å	AlInAs		35	0.42	
28 Å	InGaAs		35	0.6	
19 Å	AlInAs		35	0.42	
25 Å	InGaAs		35	0.6	
20 Å	AlInAs	1×10^{17}	35	0.42	
24 Å	InGaAs	1×10^{17}	35	0.6	
22 Å	AlInAs	1×10^{17}	35	0.42	
23 Å	InGaAs	1×10^{17}	35	0.6	
28 Å	AlInAs		35	0.42	
22 Å	InGaAs		35	0.6	
40 Å	AlInAs		35	0.42	Injection barrier
13 Å	InGaAs		35	0.6	
13 Å	AlInAs		35	0.42	
51 Å	InGaAs		35	0.6	
13 Å	AlInAs		35	0.42	

45 Å	InGaAs		35	0.6	
14 Å	AlInAs		35	0.42	
40 Å	InGaAs		35	0.6	
23 Å	AlInAs		35	0.42	

3.3.1 Wannier-Stark levels

The following graph shows conduction band structure at a given electric field and the Wannier-Stark energy levels across the structure. As can be seen from the graph, each period of the active layer consists of an electron injector and an active region where the photon is produced. The electron injector is doped at 1×10^{17} cm^{-3}. These are the default values of the structure and the next chapter will talk about the fabrication of this structure and the experimental results.

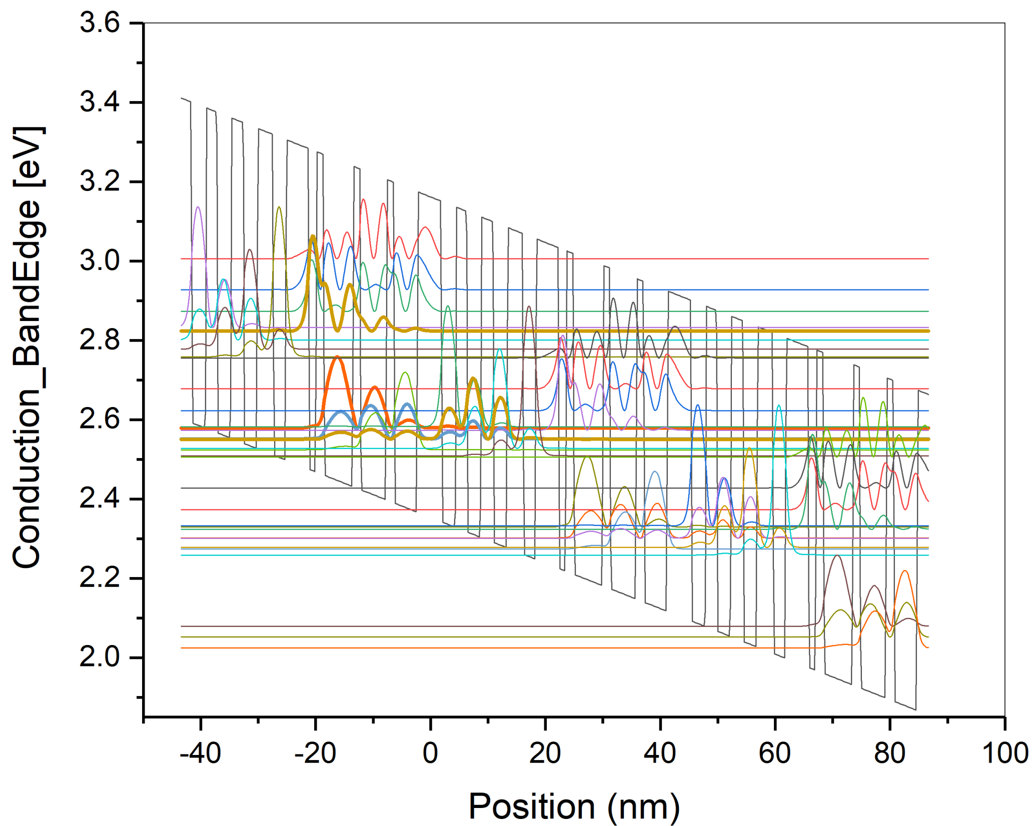

Fig 3.3.1 Wannier-Stark levels of the simulated QCL structure

The wave functions in the diagram were calculated from Schrodinger Equation by nextano and the amplitude represents the probability of finding an electron in a specific position. As mentioned before, the calculation is based on single-band effective mass Schrodinger Equation in real space for the energy levels. The calculations are self-consistent with many iterations until convergence is reached. The emission wavelength could also be deduced from the difference between energy levels where the actual transition happens (The first two bold energy levels). This will enable the future design of device emitted at targeted wavelength.

3.3.2 Gain characteristics

From the simulations, the gain spectrum is plotted along with the photon energy. The emission wavelength can also be obtained by finding corresponding photon energy at the maximum gain.

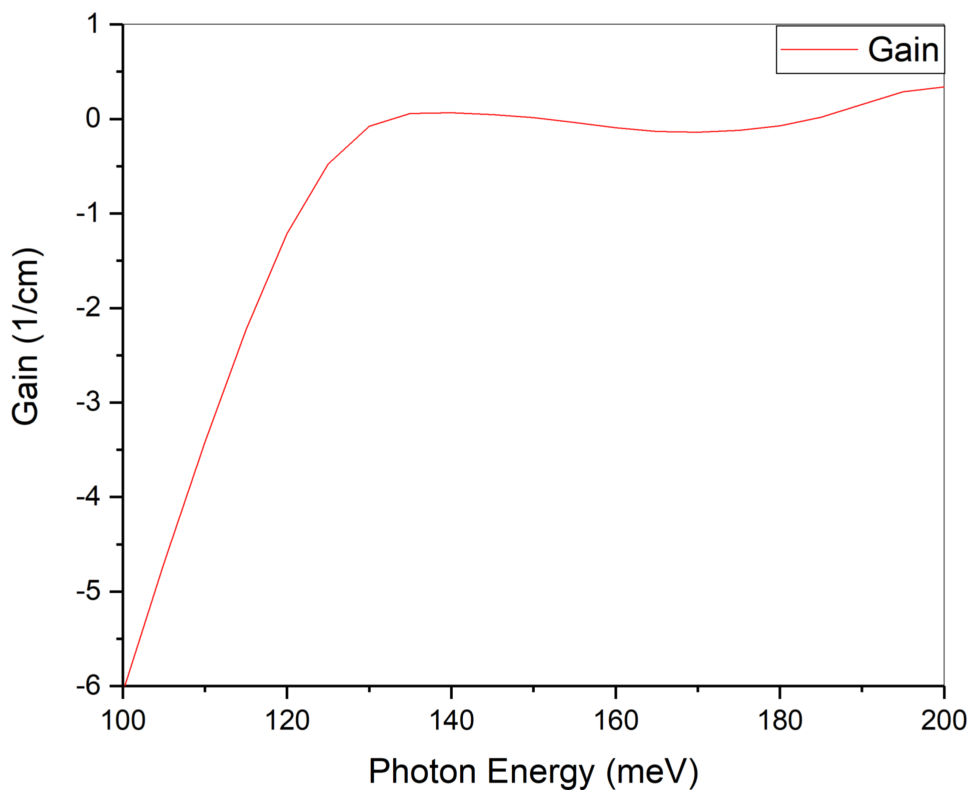

Fig 3.3.2 The gain spectrum of the simulated QCL

The gain spectrum shows that the maximum gain occurs at 200 meV, corresponding to an emission energy of 6.2 μm. This result does not match with the predicted value and the wavelength deduced from the previous wavefunctions very well. Therefore, there might be a higher gain above 200 meV. Unfortunately, as the default limit of photon energy to be simulated is 200 meV and the simulation is completed at the end of my study, the simulation of gain spectrum at higher photon energy was not able to be done. The error of this simulation is about 8% compared with expected value (5.7 μm). However, 200 meV is the last value on the x-axis, there might be a further increase after this point. Therefore, more simulation might be necessary to investigate whether there is a higher gain. Apart from this, there could be multiple reasons for this error:

(a) The simulation tool used by structure designer is different and the parameters are slightly different with that employed in Nextnano.

(b) 1 nm of difference in layer thickness can cause the change in emission wavelength, as shown in the following figure taken from reverence [5]. Figure 3.3.3 shows the gain characteristics of the QCL when the second active well thickness is changed from 4.1 to 6.1 nm. One can see from Fig 3.2.3 that a tiny change (1nm) in the well thickness can lead to dramatic change in wavelength. From calculation, one can obtain that when the well width increases from 4.1 nm to 5.1 nm, the wavelength is changing from 8.8 μm to 6.8 μm.

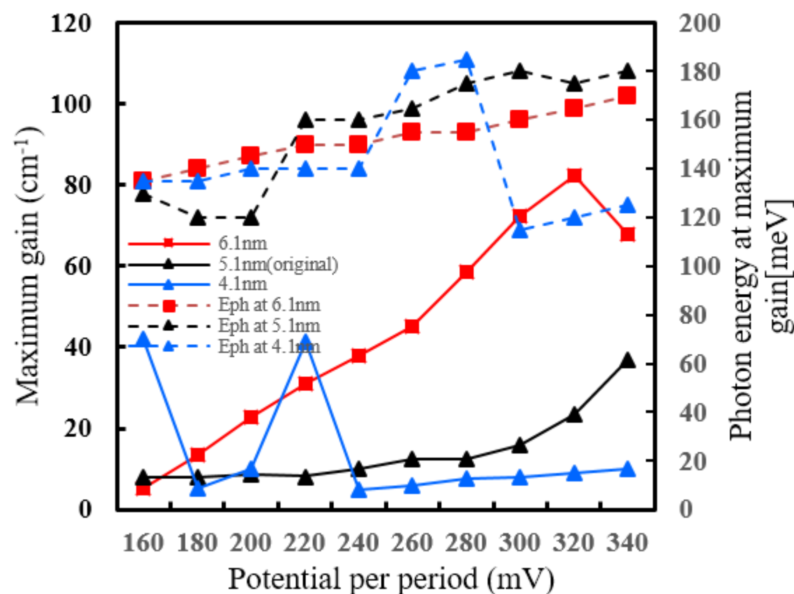

Fig 3.3.3 The gain spectrum of a QCL at different well thickness

3.3.3 IV characteristics

In order to have a better comparison with our experimental work, the IV curve has also been modelled. Fig 3.3.4 shows the IV characteristics obtained from Nextnano.

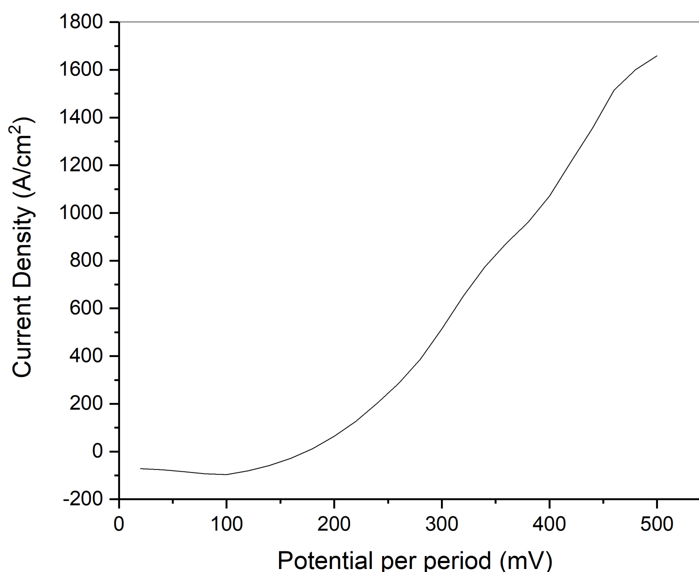

Fig 3.3.4 The IV curve of our simulated structure

As the x-axis represents potential per period, therefore we can determine the turn-on voltage for devices with different number of periods (N). For the device with 35 periods, the turn-on voltage is 5.25 V. For the device with 42 periods, the turn-on voltage is 6.3 V.

Conclusion:

Having established basic understanding on ICLs from the literature review, we have done some simple simulations on ICL structures within Nextnano to investigate the effect of electric field on carrier distribution. Our simulation shows that he increase of electric field will lead to the movement of electrons in the wells, and thus will affect the actual emission wavelength, which supports the explanations given in the literature. This could help us to well understand the significance of Stark effect on the tunability of lasers by extending the wavelength through appropriate engineering of electron distribution. Therefore, this would contribute to the design of ICLs with a large tunable range by controlling the distribution of electron.

Moreover, in order to obtain more understanding on previously designed and grown QCLs, simulations of our previous designed structure have been done by Nextnano.QCL, a GUI module specifically designed for the simulation of QCL. The band structures were modelled to

show the energy separation between energy levels and we attempted to calculate the transition energy through the band diagrams. Besides, the simulation provides the information of IV characteristic and the gain spectra as a function of photon energy. The highest gain from the graph corresponds to the photon energy of 200 meV, 6.2 μm. The results obtained by Nextnano.QCL is accurate enough and showed a good agreement with the expected design. These results will be compared with our experimental work in the next chapter.

Chapter 4 Experiments on broad area and narrow ridge lasers

4.1 Fabrication and testing of a broad area QDLs

To compare simulation results with real QCL structures, devices were grown by MOVPE and fabricated into lasers in the University of Sheffield cleanrooms. Since the fabrication of QCLs is challenging and results are sensitive to process variations, initially training was conducted on a set of Quantum Dot lasers emitting around 1.2 micron. Results of the fabrication of these lasers is shown here.

Four samples from four different wafers (labelled as TS 2375-1, TS 2375-2, TS 2376-1, TS 2376-2) were fabricated into broad area lasers. TS 2375-1 and TS 2375-2 have 5 InAs quantum dot layers in the active region, while the others have 3 quantum dot layers. TS 2375-1 and TS 2376-1 are both 3° off axis (substrate miscut) whereas TS 2375-2 and TS 2376-2 are both on axis. The substrate miscut could produce nanosteps on the surface of GaAs to form terraces as the structure is grown.

The fabrication process is detailed below:

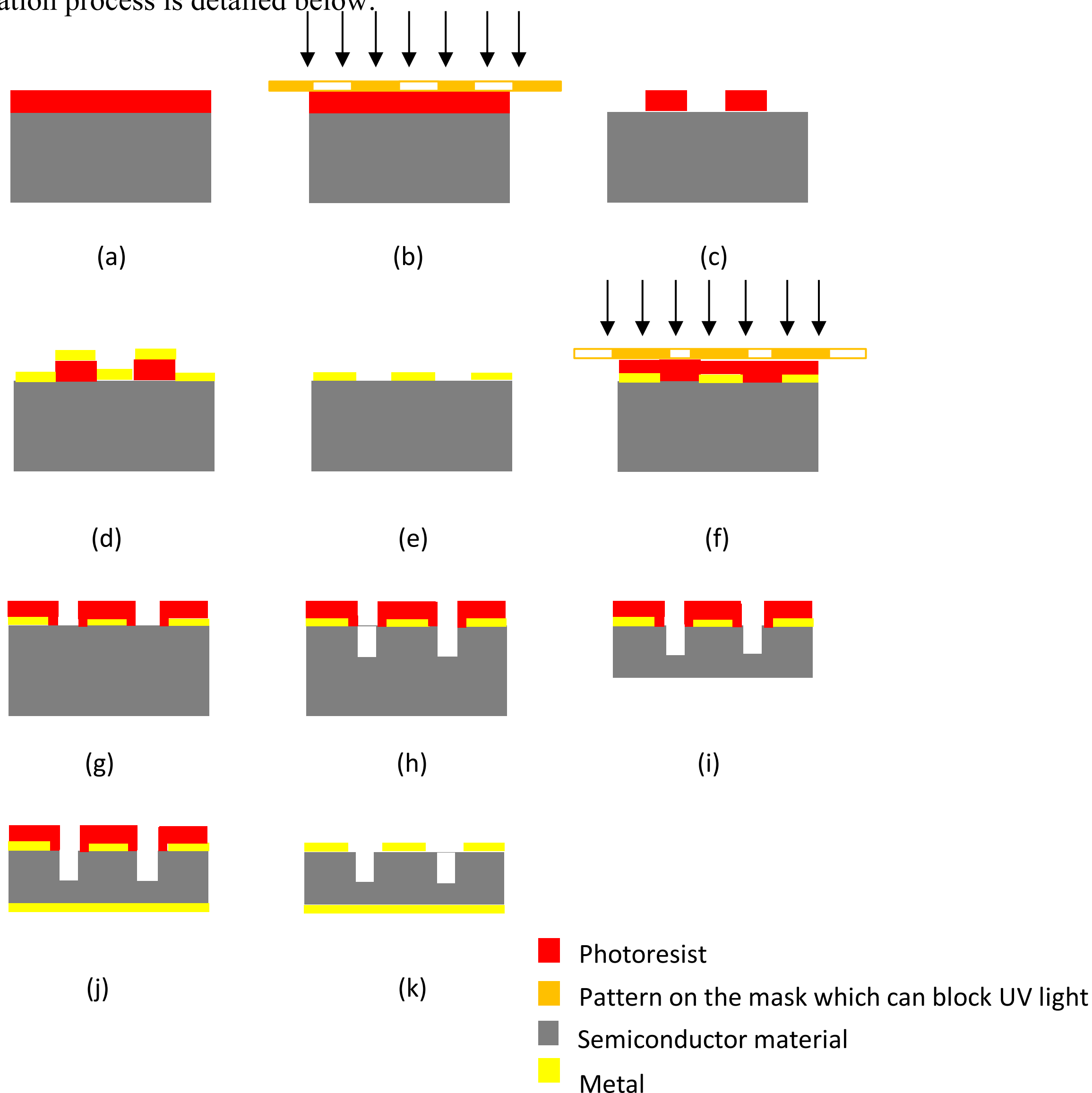

(a) Photoresist is spun on the sample. (b) Contact photolithography. (c) The sample exposed under UV light is then developed by MF26A. (d) Evaporator is used for contact metallisation. (e) After metallisation the sample is then put into acetone to remove unwanted metals. (f) Another exposure is needed to protect the metal contact prior to etching. (g) The exposed area is removed by developer MF26A. (h) Wet etch by using H_2SO_4 H_2O_2 H_2O (1:8:80). (i) The backside is then grinded by MINIMET. (j) The backside is then deposited with InGe/Au for the back contact. (k) All photoresist is removed.

Table 4.1.1 Standard QDL fabrication sheet

<table>
<tr><th>Proc. No.</th><th>Equipment/ Chemicals</th><th>Notes</th><th>Procedure</th></tr>
<tr><td>1</td><td>Scriber
1) n-Butyl
2) Acetone
3) IPA
Asher</td><td>Boil n-Butyl
Never heat Acetone</td><td>CLEAVE and CLEAN
Followed by 5 minutes Ash</td></tr>
<tr><td>2</td><td>Mask aligner 3

HMDS (adhension promoter)

PMGI

Resist = SPR350</td><td></td><td>CONTACTS PHOTOLITHOGRAPHY
Bake sample for 7 minutes after spinning with PMGI to hadern the surface
Always bake sample for 1 minute after spinning with photoresist
Get rid of the photoresist on all edges first
Mask number:
Exposure time: 13s
Follow lithography with 1 minute Ash
Inspect under Microscope</td></tr>
<tr><td>3</td><td>Thermal Evaporator 4</td><td>19:1 DIW:ammonia wash prior to loading.</td><td>CONTACTS METALISATION
Wait 20 minutes to warm up the machine
After loading, leave it for two hours to reach right pressure
Check the crystal monitor is in a good condition
<table>
<tr><th></th><th>AIM</th><th>Actual</th><th>UNITS</th></tr>
<tr><td>Au</td><td>5</td><td></td><td>nm</td></tr>
<tr><td>Zn</td><td>20</td><td></td><td>nm</td></tr>
<tr><td>Au</td><td>200</td><td></td><td>nm</td></tr>
</table></td></tr>
<tr><td>4</td><td>Acetone</td><td></td><td>Lift-off
Can expose under UV light for a relatively long time to remove all remaining photoresist
Follow with 3 solvents clean and 2minutes Ash</td></tr>
<tr><td>5</td><td>Mask aligner 2

HDMS

Resist = SPR350</td><td></td><td>SECOND PHOTOLITHOGRAPHY
Always bake sample for 1 minute after spinning with photoresist
Get rid of the photoresist on all edges
Mask number:
Exposure time: 11s
Follow lithography with 2 minutes Ash
Inspect under microscope</td></tr>
<tr><td>6</td><td>H_2SO_4
H_2O_2
H_2O
1:8:80

DEKTAK

3 Solvents</td><td></td><td>SEMICONDUCTOR ETCH (Wet etch)
<table>
<tr><th></th><th>MIN</th><th>AIM</th><th>UNITS</th></tr>
<tr><td>Etch depth = (Excluding resist)</td><td>2.1</td><td>Around 3.7 to ensure the active region is etched through</td><td>µm</td></tr>
</table>
DEKTAK 800 um scan length and 65.5um measurement range
Follow etch with a good 3 stage clean and 3minutes Ash.</td></tr>
</table>

7	MINIMET (mechanical thinining machine) FORCE:5 Speed :030 Soft stop 45 minutes per sample	3µm grit Around 45 minutes per sample	**BACKSIDE THINNING** AIM: 120 / ACTUAL: Normally 130~180 / UNIT: µm To improve the heating dissipation of the structure Respin a thick layer of photoresist to protect the front side before doing backside thinning Mount the sample on the metal block by melting a small piece of wax Be aware of uniformity, and allow for wax in thickness measurement. Three point measurement to ensure the accuracy Always check the settings Following with 3 stage clean and 3 minutes ash
8	Thermal Evaporator		**BACKCONTACT METAL** Wait 20 minutes to warm up the machine After loading, leave it for two hours to reach right pressure InGe: AIM 20 / ACTUAL 20.5 / UNIT nm Au: AIM 200 / ACTUAL 202 / UNIT nm

Table 4.1.1 outlines the standard procedures of broad area QDL fabrication. The process starts with 3-stage cleaning by n-Butyl, acetone and IPA, and then followed by 5-minute oxygen ash. The cleaned sample is then taken into yellow room to spin with photoresist. The speed of spinning is set to 4000 rpm. After baking on the hot plate and placed onto the spin coater, the sample should be blown by nitrogen gun to make sure the surface is clean. The hexamethyldisliazane (HMDS) which acts as an adhesion promoter, is first spun onto the sample. Then a few drops of PMGI should be spun on, which can make the lift-off easier after thermal evaporation. The sample is then baked for 7 minutes before coating with photoresist. After that, SPR-350 (photoresist) is spun onto the surface of the sample, and then it is further baked for 1 minute. It is important to get rid of the photoresist on the edge of the sample, because the photoresist on the edge is always thicker due to centrifugal force and the edge-bead effect which is independent of the geometry of the substrate. The edge-bead effect is caused by viscosity and surface tension of the fluid coating the surface as well as the spin recipe. After the removal of the photoresist on the edges, the sample is then aligned with the mask under the microscope of mask aligner UV 300 and exposed under UV light for 13 seconds (exposure time is subject to change). After the alignment, the sample is then developed for 1 minute with

MF26A, and dipped into deionised (DI) water. Afterwards, it can be ashed for 1 minute and inspected under microscope whether the features on the surface look good.

The sample is now ready for the evaporation of top contact, but before that, the sample should be cleaned by 19:1- DI water: Ammonia to remove the surface oxide. The tungsten coils which are used to hold the metals should be boiled with n-Butyl at the same time. Then the coils and metals can be loaded into the thermal evaporator. There are two pumps in the thermal evaporator: backing pump and diffusion pump. It is recommended to check the connections of the coils and the condition of the crystal monitor before pumping down to the desired pressure. If everything is correct, leave it for about two hours to reach desired pressure. The metals Au/Zn/Au with thickness of 5/20/200 nm are then deposited on the surface. The thickness is monitored by crystal monitor. Once the expected thickness is reached, switch off the current and close the shutter.

After metal evaporation, the sample is then put into acetone for a few minutes to allow the photoresist to react with the acetone, and thus the unwanted metal can easily be removed. Now the sample can be exposed under UV light for a long time to remove all remaining photoresist and followed with 3-stage cleaning and 2-minute oxygen ash. In order to protect the laser bars by covering them with photoresist for wet etching. A second alignment is then required. The sample is then taken to yellow room again and baked on hot plate before loading on to the spin coater. The procedure is the same as first alignment but no PMGI is needed this time because there is no lift-off process afterwards. Again, the photoresist on the edges are removed first and then the sample is aligned under mask aligner UV 400. The exposure time for this aligner is about 11 seconds, and again subject to change. The second alignment should be good enough to ensure the laser bars are well protected by photoresist. After the sample is exposed and developed, it is then followed with a 2-minute oxygen ash. The quality of the second alignment should be checked under the microscope.

The etching is done by rinsing the sample into the etchant, which is formed with 1:8:80 H_2SO_4: H_2O_2: H_2O. The ratio of H_2O_2 can be altered to control the rate of etching. The sample should be scanned with Dektak across the surface to measure the thickness of the trench and calculate how deep we need to etch down. The measurement is repeated until the aim depth is reached. The sample is then cleaned with 3-stage cleaning and followed by 3-minute oxygen ash.

In order to improve the heat dissipation, it is necessary to thinning the substrate with Minimet. Firstly, the sample is respun with a thick layer of photoresist to protect the top surface and then

mounted on a metal block upside down by melting some wax. It is taken into semi-cleanroom for the backside thinning. The thickness of the whole sample should be measured beforehand by micrometer to calculate the desired thickness. The sample is then smeared with a certain amount of 3-micron paste and loaded into the machine. Lubrication is used before switching on the machine. The thickness of the sample should be measured and recorded after every run until the aim thickness is approached.

After the backside thinning, the sample is taken back into the clean room and soaked into hot n-Butyl until the sample can come off from the metal block. A 3-stage cleaning and 3-minute ash should be followed after the sample is taken off. The sample should be held very gently because it is very fragile. After that, the InGe/Au with thickness of 20/200 nm back contact should be evaporated onto the backside of the sample. The procedure is the same as that of top contact deposition. Finally, the sample should be annealed by rapid thermal annealer (RTA) at 360℃ for 30 seconds. The process is end up with the ball bonding.

4.2 Characterisation of QDL

The fabricated devices were tested both under CW operation and pulsed operation. In CW operation, two sets of Power-Current-Voltage (L-I-V) curves were obtained: 10 mA with 0.1 mA steps and 100 mA with 1 mA steps. In pulsed mode, the current is from 0 to 1000 mA with 10 mA steps, and the laser is characterised at 1 μs at 1 %. Our devices are in the width of 50, 80, and 100 μm, and they were marked as “Small”, “Medium”, and “Large” respectively.

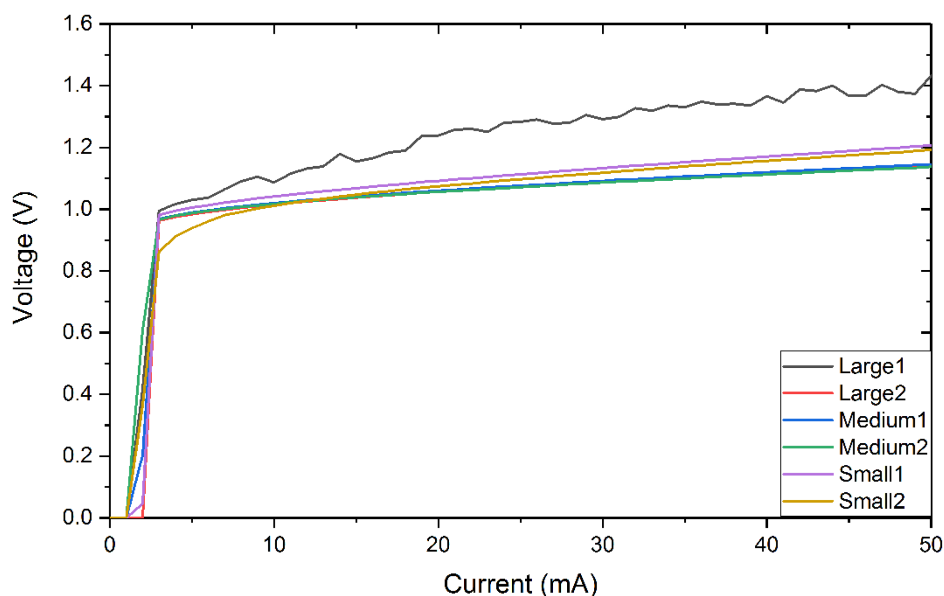

(a)

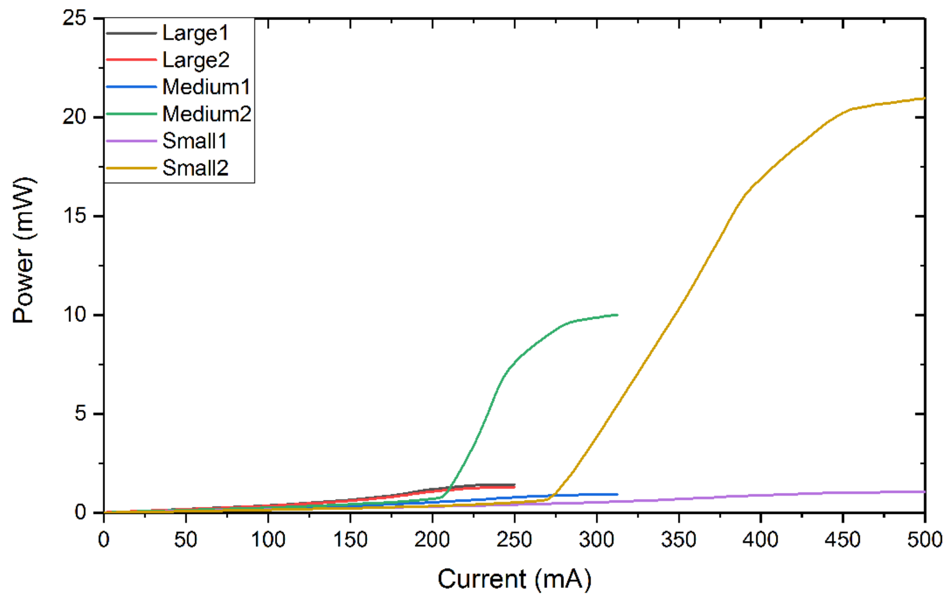

(b)

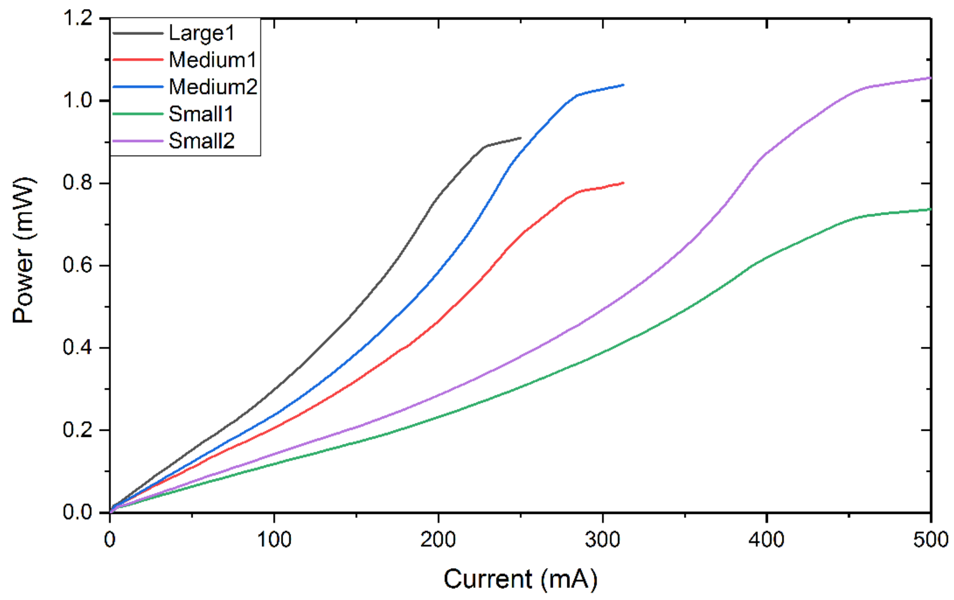

(c)

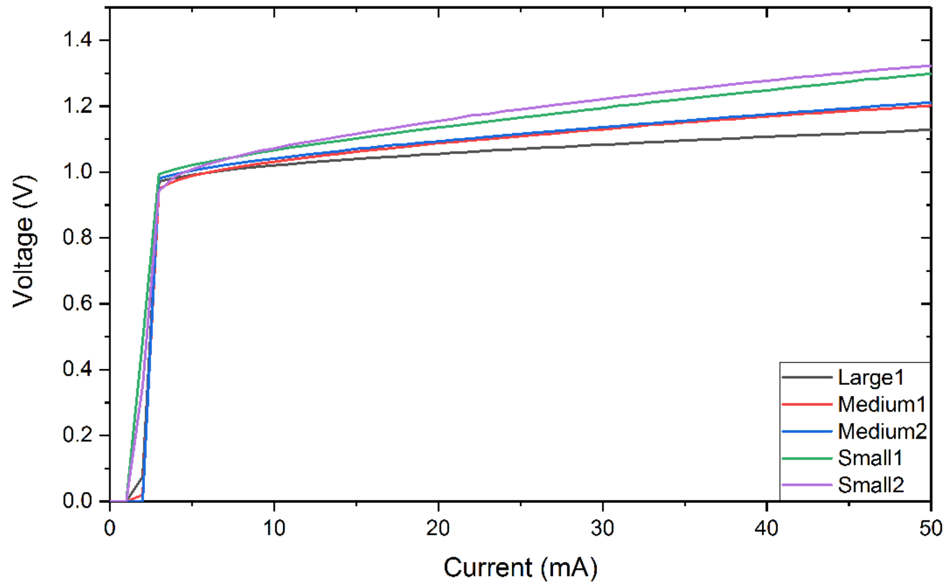

(d)

Fig 4.2.1 L-I-V curve of the sample fabricated from wafers with 5 QD layers (a) I-V curve in CW mode for TS2375-1 (b) L-I curve in pulsed mode for TS 2375-1 (c) L-I curve in pulsed mode for TS 2375-2 (d) I-V curve in CW mode for TS 2375-2.

Fig 4.2.1 demonstrates the I-V characteristics of the samples made from TS-2375-1 and TS-2375-2 in CW mode and the L-I curves in pulsed mode. According to the result, lasing only occurred in pulsed mode and only the samples with 3˚off axis were able to lase. The I-V curve in CW mode is still of interest to observe the electrical performance of those devices. Basically the I-V curves looks fine, although some noises can be found for certain devices.

The lasers which were fabricated from the off-axis wafers were able to lase at room temperature (RT). For TS 2375-1 that consists of 5 QD layers, a 4-mm-long and 80-µm-wide device lased at 300 K with threshold current density of 220 mA/cm^2, the output power is about 10 mW. A 50-µm device with the same cavity length lased at RT with a slightly higher threshold density of 270 mA/cm^2. The output power reached 20 mW.

For TS 2376-1 which consists of 3 QD layers, a 4-mm-long and 50-µm-wide device had a threshold current density of around 370 mA/cm^2, with an output power of 5.5 mW. The output power is much lower than that of the lasers with 5 QD layers.

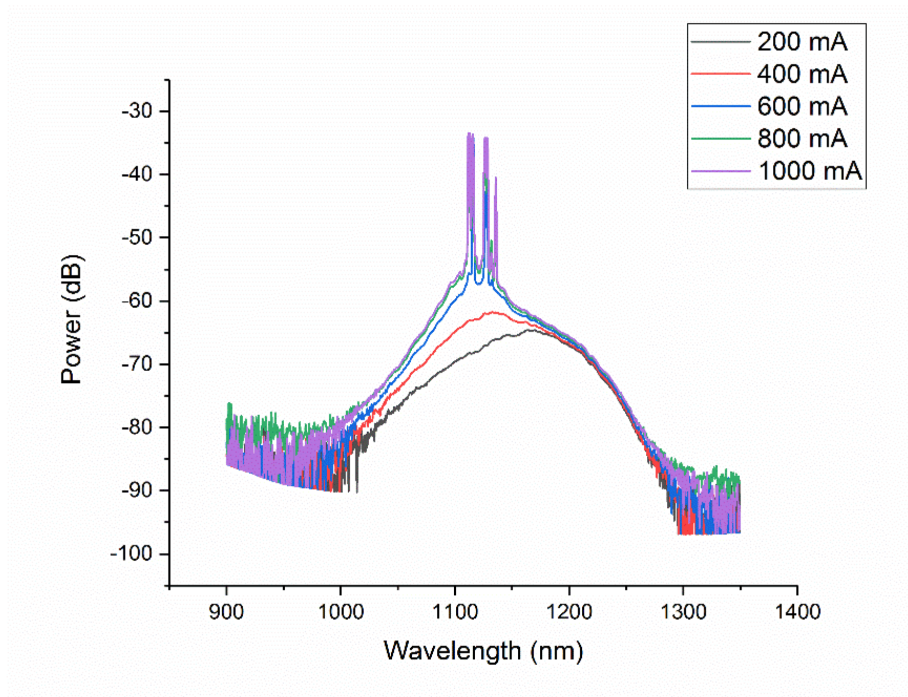

(a)

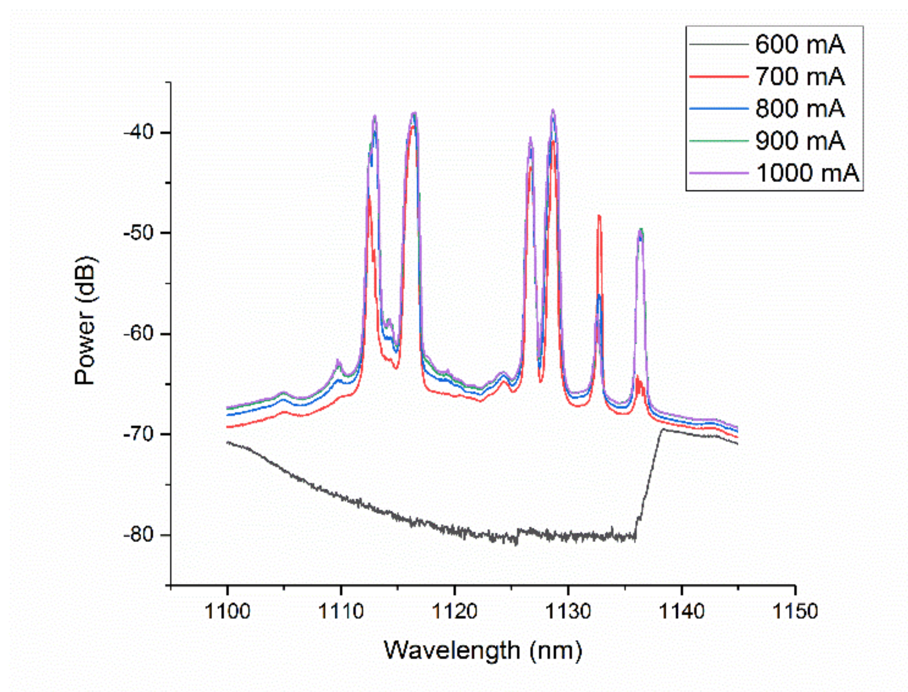

(b)

Fig 4.2.2 Spectra of the "4-mm-long and 50-μm-wide" device made from TS 2375-1 (a) broad scan (b) narrow scan across the peaks.

Fig 4.2.2 shows the spectra of the device labelled as "small 2" for TS 2375-1. The lasing wavelength centred at 1125 nm and covered from 1113 nm to 1136 nm, which was very broad.

The power was taken from the spectrometer, which was already normalised. Low temperature analysis could be taken to determine whether it is ground state or excited state lasing. The amplified spontaneous emission (ASE) experiences a blue shift with increasing injection current, depicting bias-dependent spectra. The possible cause is the carrier distribution in the quantum dots ensemble and the large distribution of dot sizes, which leads to the inhomogeneous broadening. There is a discontinuity in the 600 mA (below-threshold) curve, which could be due to the environmental noise during the measurement. In addition, a reduced threshold current current density and a redshift in the room temperature lasing was observed for the 5-layer device comparing with the 3-layer device, indicating an increased portion of lasing from ground state. The spectra for other devices which are not presented here shows similar characteristics. This could be attributed to the different sizes of quantum dots which would give rise to a broad gain width. If the size of the quantum dots are uniform, then a relative sharp spectrum should be obtained. That is one aspect which could be investigated and improved in the future growth. From the spectrum, we can also work out the threshold current is between 600 and 700 mA, which is in agreement with the results from the L-I curve.

4.3 Reproducibility

After the first success of the device fabrication, the second and third attempts has been done to reproduce the QDLs. Unfortunately, a problem always occurred during the etching process. The fabricated devices from the second and third attempts were no longer lasing, despite the fact that the spontaneous emission could be observed. Some images were taken after the wet etching.

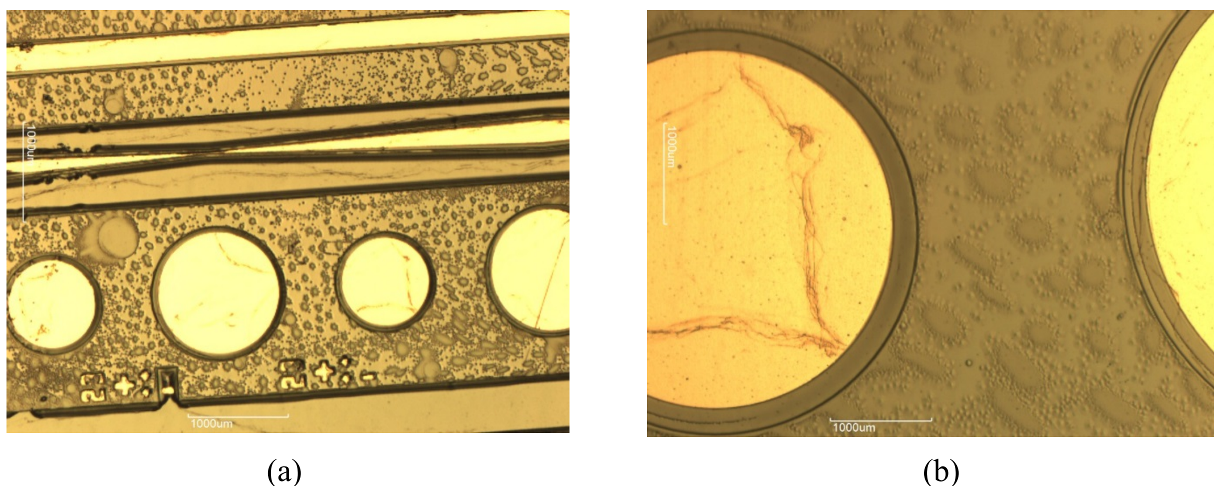

(a) (b)

Fig 4.3.2 Microscope images of the sample surface after wet etching

Fig 4.3.1 shows the condition of the sample surface after wet etching. It is obvious that the surface is in a bad condition. The defects on the surface could be the photoresist. The possible reason for that could be poor quality of the second alignment, thus the metal contacts were not well protected by photoresists.

In order to further analyse the reason for the occurred defects, some images were taken by Scanning Electron Microscopy (SEM).

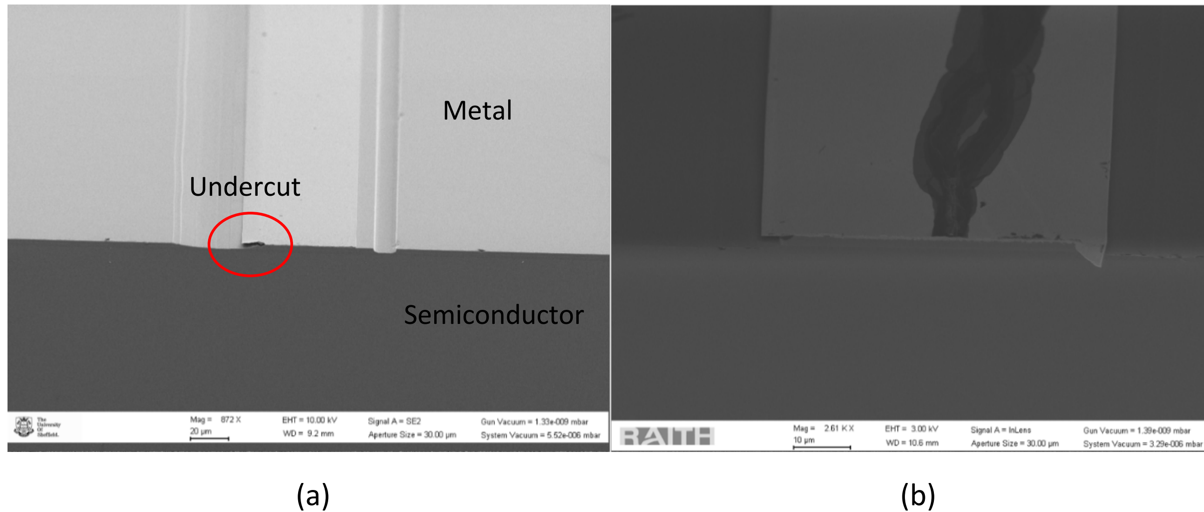

(a) (b)

Fig 4.3.2 SEM pictures of (a) the working device which was fabricated at first time (b) the device for 2nd attempt

Fig 4.3.2 compares the SEM pictures of the working device and the non-working device with bad surface condition. As can be seen from the pictures, the etchants has started reaction with the semiconductors underneath the metal contacts, forming significant undercut. This could be a possible reason for why the sample was not lasing because this may lead to poor current supply and even open circuit, although some undercuts could be observed from the working device as well. Therefore, we conclude that the bad surface condition from the second and third attempts could be due to the combination of the poor second alignment and the relative fast etching rate.

A fourth attempt was made with a slightly lower ratio of H_2O_2, the etchant now comprises of 1:4:80 H_2SO_4:H_2O_2:H_2O. A sample with 1:1:1 $K_2Cr_2O_4$:HBr:CH_3COOH etching (1:1:1 etching) was also fabricated at that time for the sake of comparison.

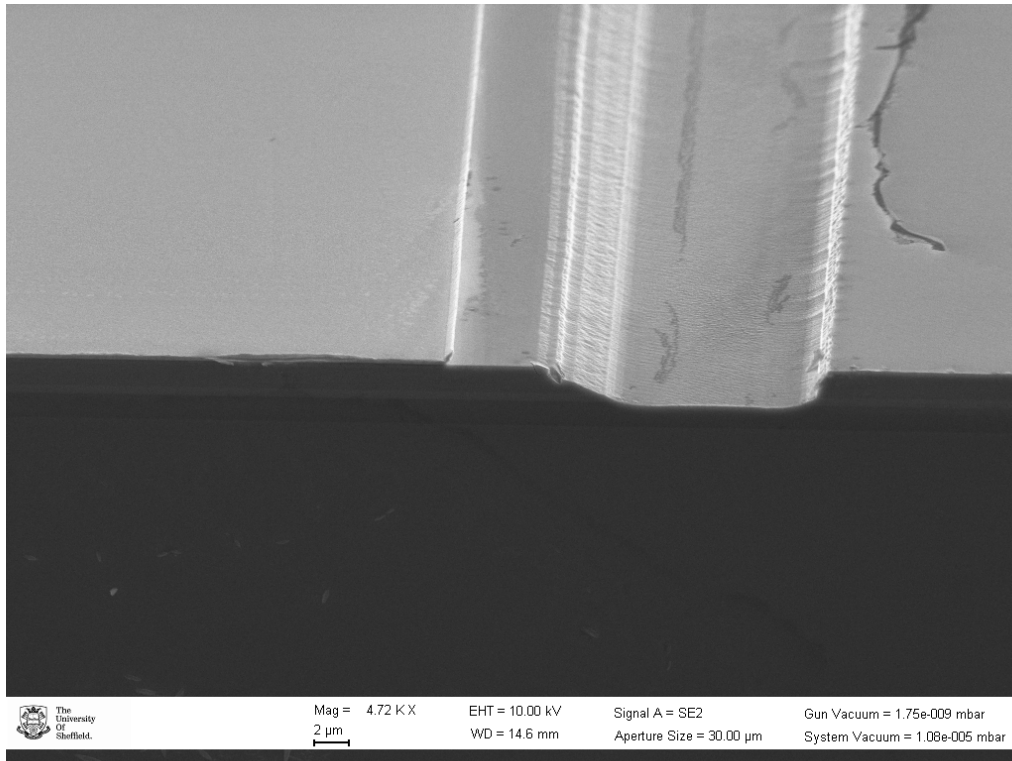

(a)

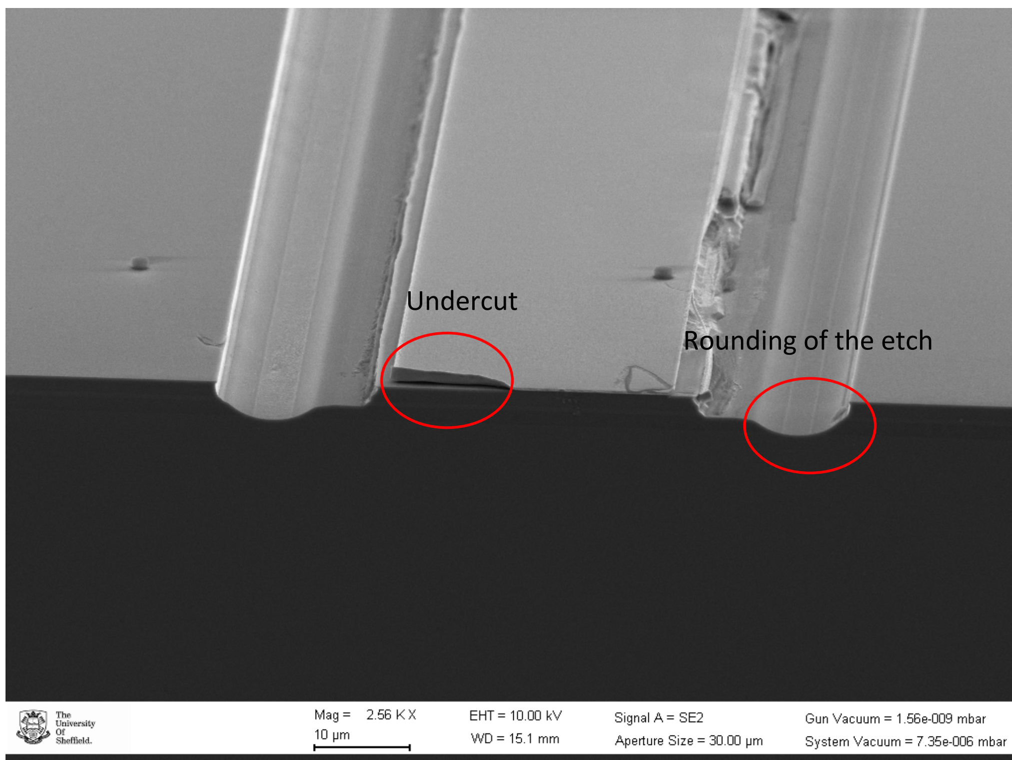

(b)

Fig 4.3.3 SEM pictures of the device with (a) 1:4:80 etching (b) 1:1:1 etching.

Fig 4.3.3 compares the SEM images of two samples using different etchant. The sample using 1:4:80 etching (Fig 4.3.3-a) has a smoother sidewall compared to the other one which was using 1:1:1 etching (Fig 4.3.3-b). Due to the very fast etching rate and the isotropic nature of 1:1:1 etching, the semiconductors were etched away very quickly and a very serious undercut of metals could be observed from Fig 4.3.3 (b). This undercut is mainly on the left side of the bar and might affect the current injection through the structure. This would then affect the quality of the laser, even it might still be able to lase in this case. However, our result showed that this device was not able to lase, meaning that the current get injected to the structure but could not spread enough under the defective bit on the left side. In addition, a rounding of the etch occurred in (b) could be attributed to the orientation of the sample. A different profile might be obtained if a different phase is exposed to the acid. Further experiment should be done to verify this assumption.

4.4 Fabrication and characterization of Narrow ridge QCLs

Having established the ability to fabricate lasers using the QDL test samples, and with training on Characterisation on lasers, the next step was the fabrication of QCL structures. Narrow ridge (5µm) InP based QCLs have been fabricated because unlike QD lasers, the threshold current density is expected to be high in QCL, hence a significant current injection would be required with subsequent problems with heat generation if broad are lasers are used. These narrow ridge QCLs were therefore fabricated to reduce the operating current and tested to examine the performance of different devices. The predicted wavelength provided by structure designer of these devices is 5.7 µm. The devices were fabricated from two 3-inch wafers (MR 3877 and MR 3881) with different periods of active regions to investigate the potential for improved threshold current with period. MR3877 was designed to have 35 periods and MR 3881 was designed to have 42 periods. Each period of the active region is composed of the superlattice of $In_{(0.6)}Ga_{(0.4)}As/Al_{(0.58)}In_{(0.42)}As$ with the thickness of 31/**18**/28/**19**/25/<u>**20**/24/**22**/23</u>/**28**/22/**40**/13/**13**/51/**13**/45/**14**/40/**23** Å. The bold script represents the AlInAs barrier, while the normal script represents the InGaAs well. Underling indicates that these layers are doped at 1×10^{17} cm^{-3}. The details are listed as below:

Table 4.4.1 The active region layer thickness of the QCL (MR 3877)

Thickness	Material	doping	repeats	In fraction	
31 Å	InGaAs		35	0.6	
18 Å	AlInAs		35	0.42	
28 Å	InGaAs		35	0.6	
19 Å	AlInAs		35	0.42	
25 Å	InGaAs		35	0.6	
20 Å	AlInAs	1×10^{17}	35	0.42	
24 Å	InGaAs	1×10^{17}	35	0.6	
22 Å	AlInAs	1×10^{17}	35	0.42	
23 Å	InGaAs	1×10^{17}	35	0.6	
28 Å	AlInAs		35	0.42	
22 Å	InGaAs		35	0.6	
40 Å	AlInAs		35	0.42	Injection barrier
13 Å	InGaAs		35	0.6	
13 Å	AlInAs		35	0.42	
51 Å	InGaAs		35	0.6	
13 Å	AlInAs		35	0.42	
45 Å	InGaAs		35	0.6	
14 Å	AlInAs		35	0.42	
40 Å	InGaAs		35	0.6	
23 Å	AlInAs		35	0.42	

Fabrication of a narrow ridge QCL is much more difficult because the ridge width is only 1/10 of that of a broad area laser. The alignment in this case requires more precise operation. In

addition, a hard mask formed of Silicon Nitride is necessary in narrow ridge QCLs and dry etch will be used. The detailed fabrication process was shown below.

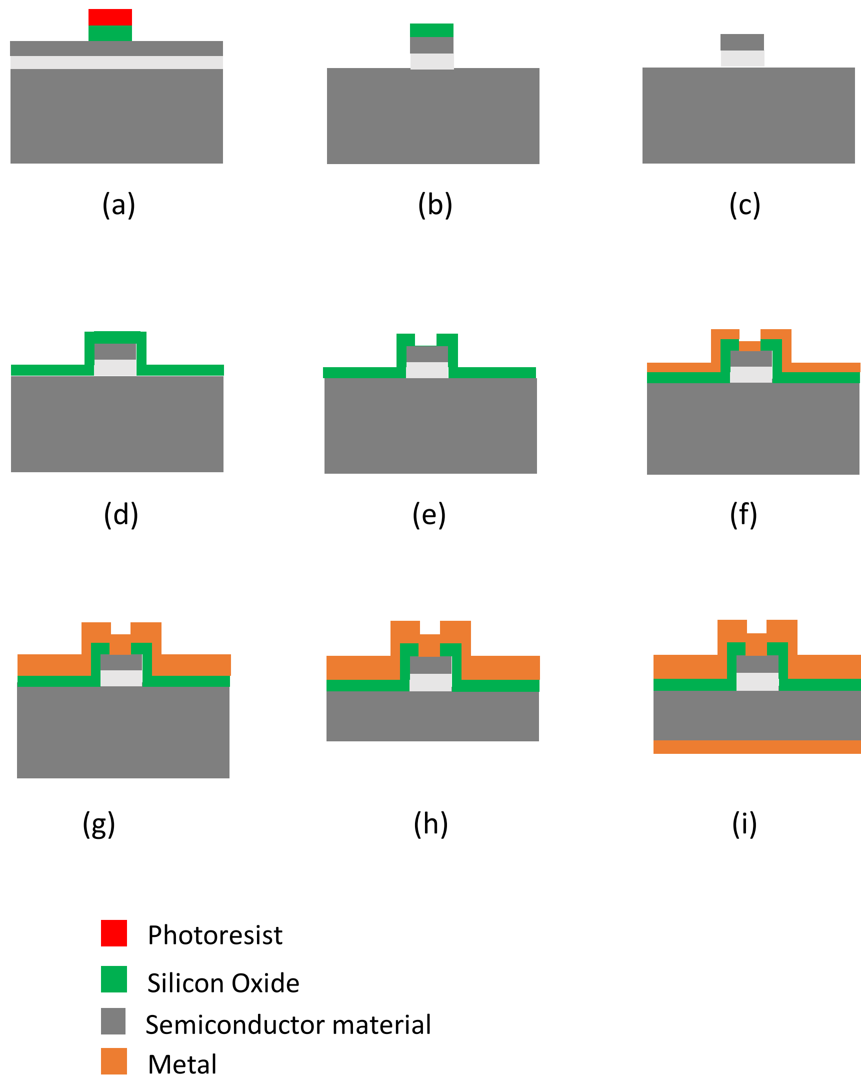

(a) The ridge is defined by photolithography and coated with Silicon Dioxide. (b) Plasma dry etch combined with wet etch. (c) The Silicon Dioxide is removed in PECVD. (d) The sample is recoated with dielectric materials for insulation. (e) The contact window is opened. (f) The sample is coated with metals by evaporation. (g) The sample is thickened by electroplating 5 micron of gold. (h) The sample is then thinned. (i) The backside is then coated with metals by evaporation.

Table 4.4.2 Standard QCL fabrication sheet

Proc. No.	Equipment/ Chemicals	Notes	Procedure
1	Scriber 1) n-Butyl 2) Acetone 3) IPA Asher	Boil n-Butyl Never heat Acetone	**CLEAVE and CLEAN** Followed by 5 minutes Ash
2	PECVD	10 min prep 600 nm (15 min)	**Silicon dioxide deposition** To form a hard mask
3	Mask aligner **3**	HMDS PMGI (makes the lift-off process easier) Resist = SPR350	**Rigde definition** Bake sample for 7 minutes after spinning with PMGI to hadern the surface Always bake sample for 1 minute after spinning with photoresist Remove the photoresist on all edges first Mask number: **Exposure time: 13s** Follow lithography with 1 minute Ash Inspect under Microscope
4	ICP	15 min prep Oxide-1 Recipe	**Hard Mask definition (Etching of silicon oxide)** Align the laser beam to the silicon oxide and keep an eye on the trace Inspect under microscope when finished
5	Photoresist stripper 3 Solvents	Stripper 3 Solvents Followed by asher	**Photoresist removal** Rinse the sample in photoresist stripper Thoroughly clean the sample by 3 Solvents 1 minute oxigen ash
6	ICP	15 min prep InP-1 recipe	**Semiconductor Etch** To form the ridge by etching trunches
7	ICP	15 min prep Oxide-1 recipe	**Silicon dioxide etch** Etch 600 nm of silicon dioxide to remove all slilicon dioxide

<table>
<tr><td>8</td><td>PECVD
3 Solvents cleanning</td><td>10 min prep</td><td>Silicon Nitride deposition
400 nm SiN to form electrical isolation
3 Stage cleanning</td></tr>
<tr><td>9</td><td>Spin coater
Mask aligner</td><td>Use SPR 350
HMDS</td><td>Contact window definition
Respin with photoresist
Edge removal
Make sure the window is on the ridge</td></tr>
<tr><td>10</td><td>ICP
3 Solvents</td><td>15 min Prep</td><td>Silicon Nitride etch
Align the laser beam to the edge and inpect the trace
Etch 400 nm of SiN to remove all unwanted SiN
Inspect under microscope to make sure the window is completely opened
3 Stage cleanning</td></tr>
<tr><td>11</td><td>Photoresist stripper
3 Solvents
Asher</td><td></td><td>Photoresist Removal
Use Photoresist stripper
Clean by 3 solvents
Followed by 2min-ash</td></tr>
<tr><td>12</td><td>Spin coater
Mask aligner</td><td></td><td>Contact pad (laser) definition
Respin with photresist SPR 350
Edge photoresist removal
Define contact pad (laser) by expose under uv light for long enough</td></tr>
<tr><td>13</td><td>Thermal Evaporator</td><td>19:1 DIW:ammonia wash prior to loading</td><td>Contacts Metalisation
Wait 20 minutes to warm up the machine
After loading, leave it for two hours to reach right pressure
Check the crystal monitor is in a good condition<table><tr><td></td><td>AIM</td><td>Actual</td><td>UNITS</td></tr><tr><td>Ti</td><td>20</td><td></td><td>nm</td></tr><tr><td>Au</td><td>200</td><td></td><td>nm</td></tr></table></td></tr>
<tr><td>14</td><td>Acetone</td><td></td><td>Lift-off
Dip the sample in the acetone for a few minutes and lift off unwanted metals
Expose under UV light for a relatively long time to remove all remaining photoresist
Follow with 3 solvents clean and 2minutes Ash</td></tr>
<tr><td>15</td><td>Power Supply
Pd mesh</td><td>To improve heat dissipation</td><td>Electroplating (5 micron Au)
Calculate the plating current
Program the power supply
Make sure correct working electrodes was connected
Switch on the vibrator
Check the charge transfer is in progress
Wait for the sequence to be completed</td></tr>
</table>

<table>
<tr><td rowspan="4">16</td><td rowspan="4">Spin coater
MINIMET
FORCE:5
Speed :030
Soft stop

60 minutes per sample</td><td rowspan="4">Use 3µm grit and lubrication liquid

Around 60 minutes per sample</td><td colspan="4">BACKSIDE THINNING</td></tr>
<tr><td colspan="2">AIM</td><td>ACTUAL</td><td>UNIT</td></tr>
<tr><td colspan="2">120</td><td>Normally 130~180</td><td>µm</td></tr>
<tr><td colspan="4">Substrate thinned to around 120µm for the further improvement of thermal dissipation
Respin a thick layer of photoresist (BPRS 100) to protect the front side before doing backside thinning
Mount the sample on the metal block by melting a small piece of wax
Be aware of uniformity, and allow for wax in thickness measurement.
Three point measurement to ensure the accuracy
Always check the settings
Following with 3 stage clean and 3 minutes ash</td></tr>
<tr><td rowspan="4">17</td><td rowspan="4">Thermal Evaporator
RTA</td><td rowspan="4"></td><td colspan="4">BACKCONTACT METAL
Wait 20 minutes to warm up the machine
After loading, leave it for two hours to reach right pressure</td></tr>
<tr><td></td><td>AIM</td><td>ACTUAL</td><td>UNIT</td></tr>
<tr><td>InGe</td><td>20</td><td>20.5</td><td>nm</td></tr>
<tr><td>Au</td><td>200</td><td>202</td><td>nm</td></tr>
</table>

Method:

The sample was firstly cleaned by three solvents (n-Butyl, acetone and IPA) followed by 3-minute ash to make sure the surface is perfectly clean. Secondly, a thin layer (600 nm) of SiO_2 was deposited on the surface of the sample to form a hard mask. Thirdly, a few drops of HMDS was coated on the sample as an adhesion promoter. PMGI was then spun onto the surface of the sample for the ease of lift-off of top contact, following by 7-minute bake on a high temperature hot plate. The photoresist SPR-350 was then spun onto the sample following by 1-minute bake on a 100 °C hot plate. The ridges of the lasers were defined by exposing the sample under mask aligner (UV 400) for about 13 seconds and dipping into the developer for 1 minute. The parts not covered by photoresist will be dry etched by ICP, forming a hard mask. The photoresist was then removed by photoresist stripper and the sample was further cleaned by three solvents (n-Butyl, acetone and IPA). After that, the exposed semiconductor and remaining silicon dioxide was dry etched respectively in ICP.

The sample was then put back into PECVD for Silicon Nitride deposition for electrical isolation. In order to form a large contact pad for the top contact. A contact window (~1.5 µm) need to be defined using mask aligner and then the window was opened by ICP dry etch. The contact pad was then defined and Ti/Au (20/200nm) was evaporated on the surface as the top contact. The sample was then placed in acetone for metal lift-off. In order to improve the heat

dissipation, a thick layer of gold was electroplated above the top contact. Electroplating is a way to plate one metal onto another for decorative or protection purposes.[1] The cathode will be the plating materials. The sample is fixed on a glass slide and tighten in to the beaker filled with Aurofab BP RTU II. The sample should be fully covered by the solution and a Pd mesh is connected to the anode. The plating current should be low enough to obtain a smooth surface. In our case, the plating current is set to be 1 mA. The whole process takes about 6 hours for plating about 5 micron of gold on the top contact.

After the top contact deposition, the sample was mounted on a metal block upside down for the backside thinning. This is to further improve the heat dissipation of this device. Once the sample was thinned enough, it was then put back into the thermal evaporator for the deposition of back contact. The back contact is composed of 20/200 nm InGe/Au. After the thermal evaporation of back contact, the sample was annealed in RTA using the recipe 360-2 (360 ℃, 30 seconds). Finally, the sample was scribed into different devices with various cavity length. The devices were mounted on ceramic tails and ball bonded. Some of the devices were also HR coated and mounted onto the copper heatsink for comparison.

Devices from different wafers (MR 3877 and MR 3881) with cavity length of 4mm were tested by pulsed current source and power detector to measure the power-current characteristics. The spectra of both samples were then taken by Fourier Transform Infrared Spectroscopy (FTIR). The FTIR should be filled with liquid nitrogen for cooling, to reach the working temperature of the detector. A lock-in amplifier was used to filter out unwanted signals.p The pulse width of the current supply was set to 1 μs, and the duty cycle was adjusted from 1% to 5%. After a full set of characterisation of different devices, a sample from MR 3877 was coated by HR materials (MgF_2). The HR coated devices were also tested, a reduced threshold current density could be observed. These results will be compared in detail.

The sample was probed to measure the IV curves first to determine whether these devices can work electrically, as shown in Fig 4.5.1. The lasers were then ready to be tested to see whether it was able to lase.

4.5 Results

The turn-on voltage of the device can be obtained by plotting a tangent line at high voltage (linear region). In QCLs, a greater number of quantum wells corresponds to a higher turn-on voltage. Therefore, the device with 42 periods is expected to have a higher turn-on voltage compared with the one with 35 periods.

Fig 4.5.1 shows the I-V curves of both samples. The device with a smaller number of periods of active regions (MR 3877) is turned on earlier than the other one, which is as expected. However, the I-V curve was only shown up to 90 mA as it was measured with CW source. Therefore, a pulsed measurement would be necessary in the future to determine the I-V characteristics up to working current.

One can see from Fig 4.5.1 that the turn-on voltage is approximately 5 volts for MR 3877 (35 periods) and 6 volts (42 periods) for MR 3881, which means the voltage is increased with the increasing of periods. These results also match up with our simulation in Chapter 3.3.3. The results are comparable and within an acceptable range.

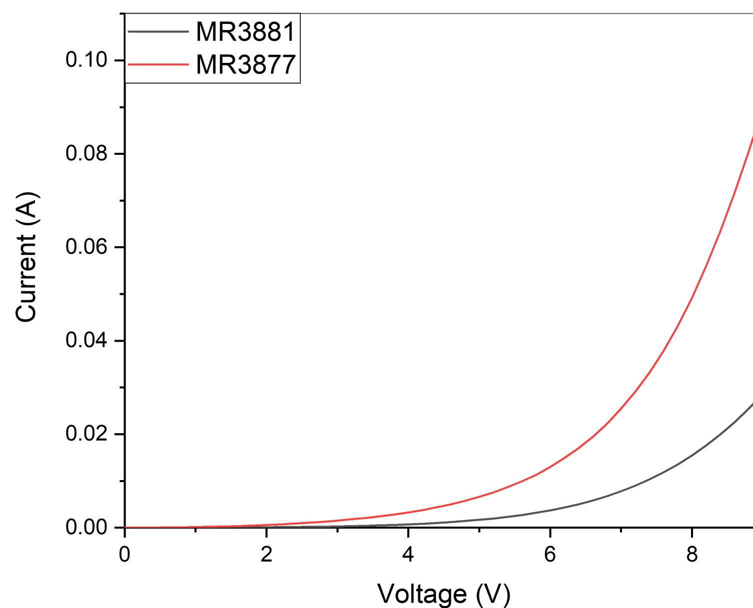

Fig 4.5.1 The IV characterisation of the QCL device

4.5.1 Power-Current (L-I) characterisation

As mentioned above, a 3-A pulsed current source was used to measure the L-I characterisation. The pulse width was set to 1µs, while the duty cycle was varied from 1% to 5%. The current was set to be 1000 mA with a step of 10 mA. Fig 4.5.2 and Fig 4.5.3 shows the L-I characteristics of 4mm devices from both wafers.

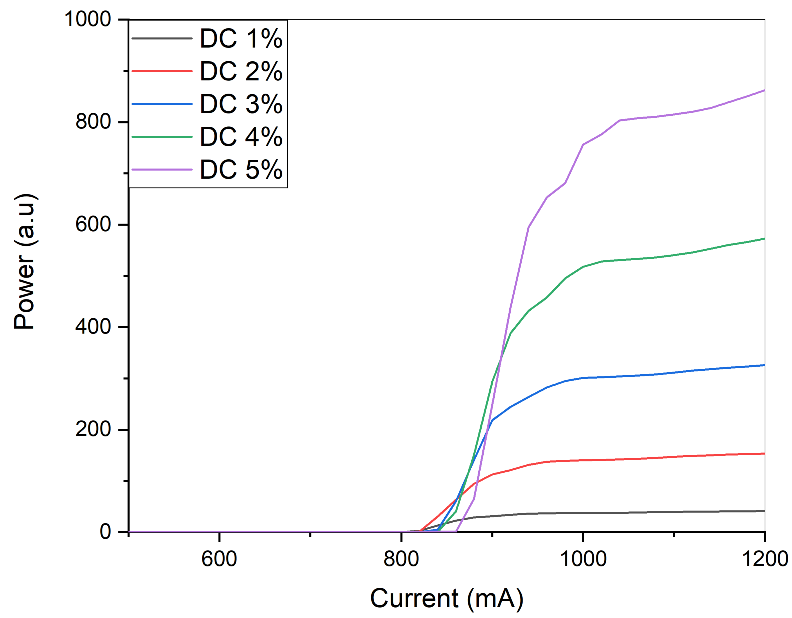

Fig 4.5.2 L-I characterisation of MR 3877 (35 periods)

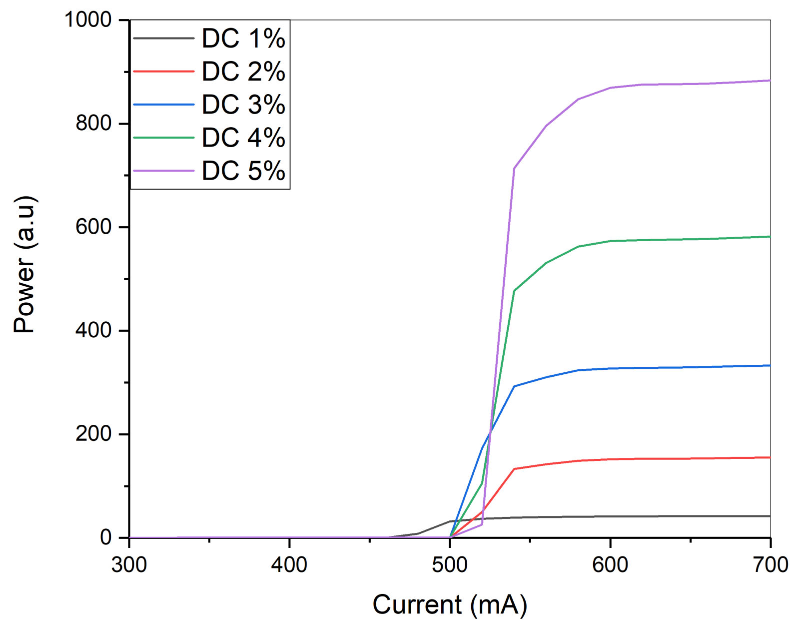

Fig 4.5.3 L-I characterisation of MR 3881 (42 periods)

The L-I curves of these QCLs shows that they are able to lase. When the threshold current is reached, the power starts to increase dramatically while the gain is clamped. However, the power saturates at a certain value, which is not normal. Normally, the power is expected to keep increasing rather than saturate after a certain current is reached. As the power increases

with the increase of duty cycle, therefore, the reason is not the saturation of detector. Instead, the saturation in output power could be attributed to the current spreading in the active region as the active region is not completely etched through. Therefore, the injected current is feeding modes from different part of the structure. This can also illustrate why the intensity of the main peak is reducing while a second peak occurs. Besides, the saturation of power could also be attributed to the increasing of loss at high current, especially the heating issue, as a laser is working based on the balance of gain and loss. If the structure is not optimal, then the power might be limited thermally at high current. However, the actual reason needs further investigation, which would be of interest for future work.

As shown in Fig 4.5.2 and Fig 4.5.3, devices made from MR 3881 have lower threshold current density, which is as expected. When period increases, the mode confinement factor and gain will increase as well. Therefore, a reduced threshold current density can be found. However, the threshold current density might not have decreased if further increase the number of periods. For instance, additional periods could lead to a misalignment of energy levels with a longer growth time. The resistance might increase with period as well, and the thicker structure might also have led to fabrication problems.

One can also see from the figures that the power increases when the duty cycle is adjusted from 1% to 5%. Besides, for the device made from MR 3877, It is worth noting that the output is not flat beyond the saturation point. The power has the trend to further go up. This can be analysed along with the spectra shown in Fig 4.5.5 . When the current is further increased, a second peak occurs next to the main peak. Therefore, the increase of power might reflect the emission from another state, which is at a higher energy.

The reduction in threshold current density can be supported by the equation below:

$$G = g\Gamma J_{th} , \qquad (4.5.1)$$

where G is the gain of the laser, g is the gain coefficient, Γ is the mode confinement factor and J is the current density. The Gain of a laser can reflect the strength of the signal amplification, which can be defined as the ratio between output and input power. The gain coefficient g is defined as the natural logarithm ratio between the output power and input power, which reflects the rate of change in output power when varying the input power.

Assuming the number of the active region in a QCL is Np, each period of the active region has a confinement factor of Γ_p, equation (4.5.1) then becomes as:

$$G = g\Gamma_p N_p J_{th}. \quad (4.5.2)$$

From the equation, Γ_p should be a constant for a certain device, it is consistent in each period. If the number of periods Np increases, a lower threshold current density Jth will be required to achieve the gain.

$$N_p(MR3877) = 35$$

$$N_p(MR3881) = 42 = 1.2\ N_p(MR3877)$$

Therefore, the threshold current density of MR3881 should be decreasing:

where,

$$J_{th}(MR3881) = 2.4\ kA/cm^2$$

$$J_{th}(MR3877) = 4.1kA/cm^2 = 1.7J_{th}(MR3881)$$

This is as expected.

The above calculation could basically reflect that the increase of period corresponds to the reduction of threshold current density. The difference could be attributed to fabrication and the loss in the cavity, assuming mirror loss is constant for all devices. This can be seen from the the following figure which shows the SEM image of our device. The fabrication is not optimal and has slight difference device by device. Therefore, this could be one reason of the error. The internal loss will be calculated later.

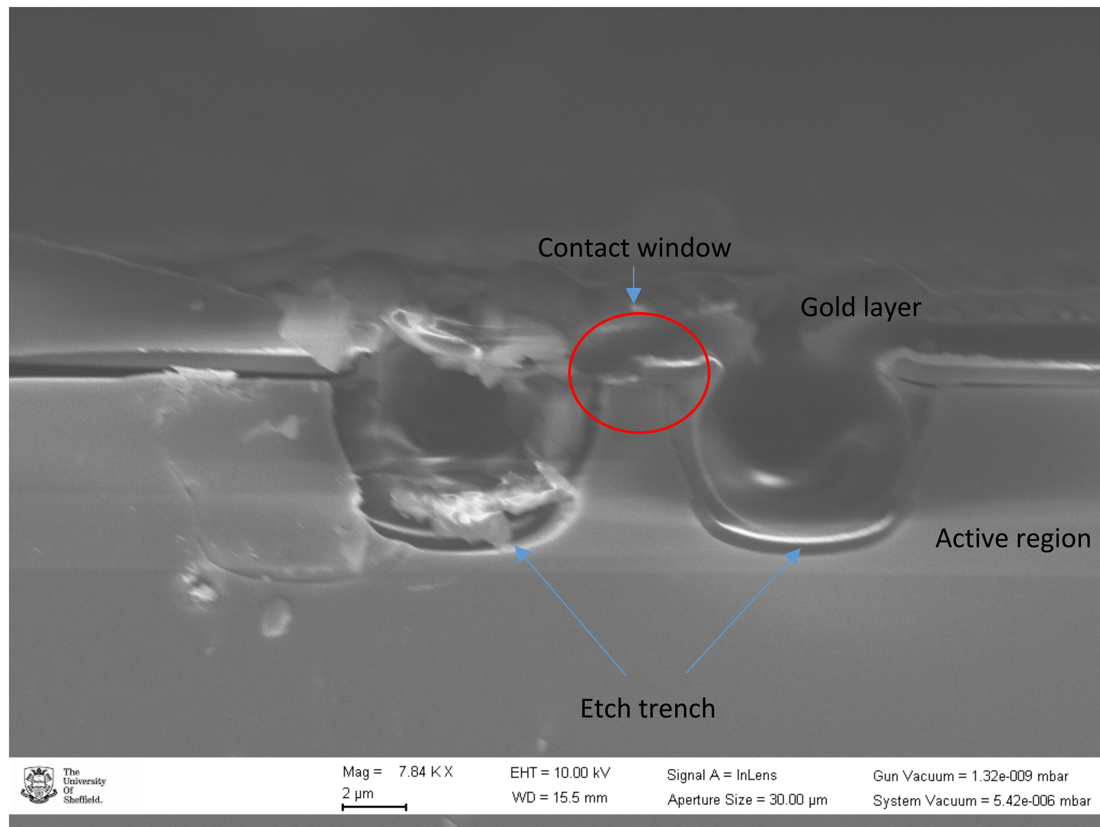

Fig 4.5.4 The SEM image of a narrow ridge QCL

As shown in Fig 4.5.4, the device has not been etched through the active region, which would lead to current spreading effects. The injection current could leak to the other parts of the structure, and the injected current might be able to feed the modes in the other parts of the structure. Besides, the light could not be confined very well in the active part of a laser. Therefore, the performance of QCL will be degraded. The window is on the top of the ridge, which connects the top contact with the device. In addition, one can see that there is a very thick electroplated gold on the top. Ideally, the window should be in the middle of our ridge but in our case, the window is not clear enough to see and it is not exactly in the middle. A perfect device should have a 1.5-μm contact window in the centre of a 5-μm ridge. This could affect the connection between the contact and our device.

Table 4.5.2 The relationship between threshold current density and duty cycle

Duty cycle	1%	2%	3%	4%	5%
I_{th} (mA)	820	820	840	860	880
J_{th} (kA/cm^2)	4.1	4.1	4.2	4.3	4.4

Table 4.5.2 demonstrates how the threshold current density varies with the change of duty cycle. Obviously, the threshold current density is going up while the duty cycle increases from 1% to 5%, meaning that when the current supply is getting close to continuous wave mode, the device generates more heat, leading to the increase of threshold current.

4.5.2 Spectra analysis

The spectra were taken by FTIR spectrometer. The average time to run a complete measurement for our devices were 7 minutes. Liquid nitrogen should be applied regularly to cool down the sensor in the FTIR. A laser beam was emitted from the FTIR and reflected by two face-to-face mirrors and finally the laser beam will be aligned with our device to take the spectra.

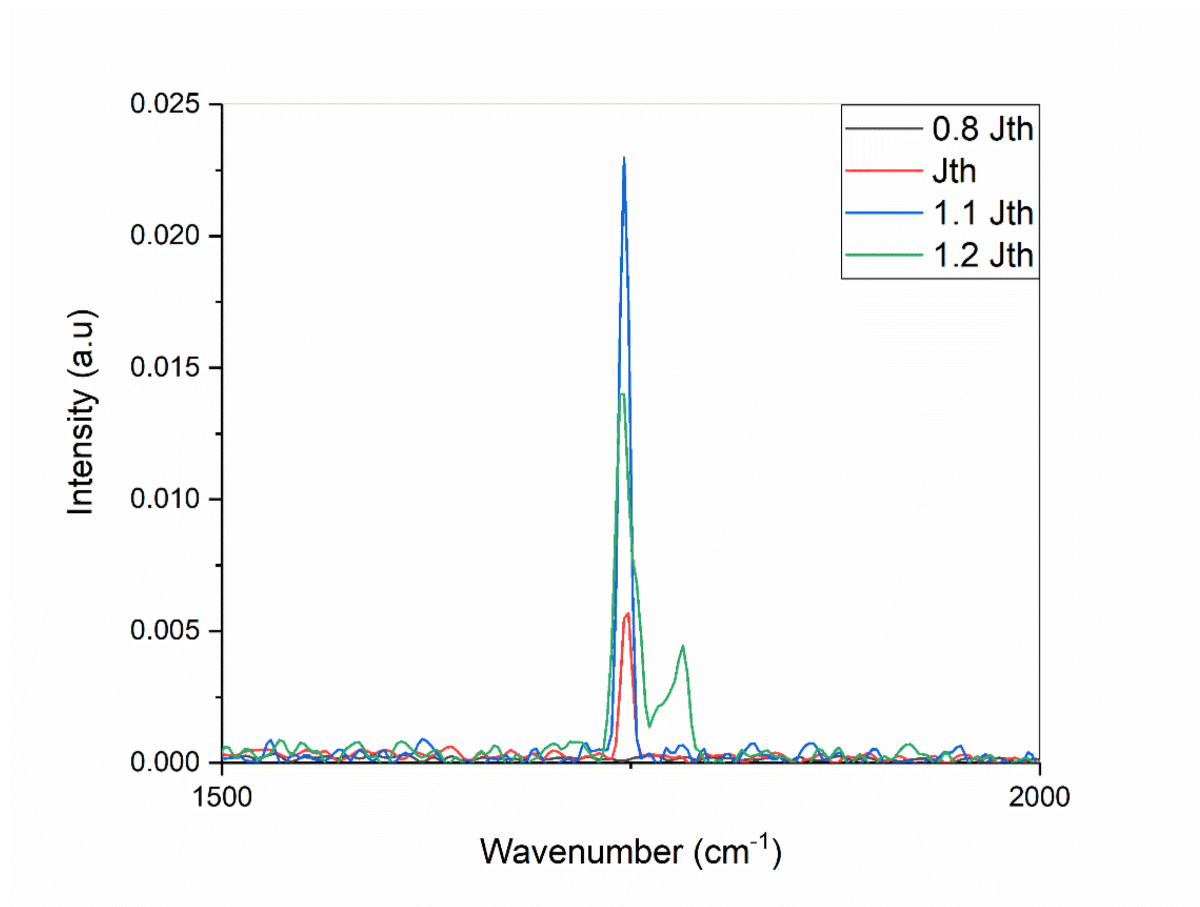

(a)

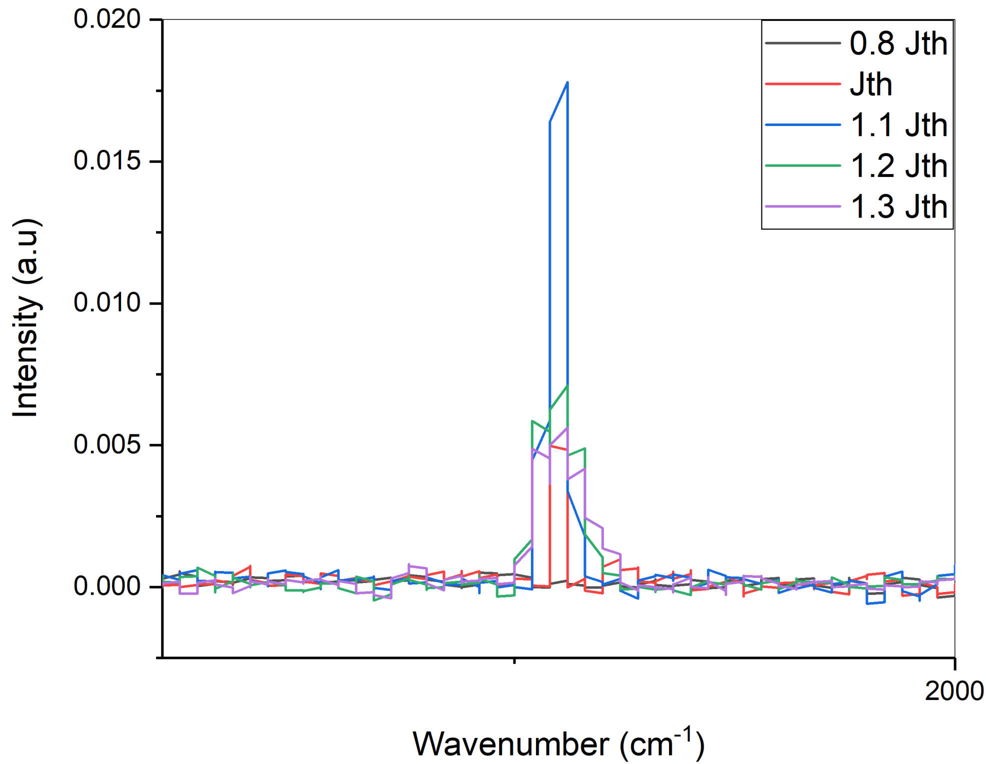

(b)

Fig 4.5.5 Spectra of the narrow ridge QCLs with 35 periods (a) and 42 periods (b)

Fig 4.5.5 shows the spectra of the 4mm devices made from MR 3877 and MR 3881. From calculation, the emission wavelength of these lasers corresponds to the predicted value, which is 5.7 μm.

It is significant that the highest intensity for the main peak occurs at 1.1 Jth. The intensity of main peak is reducing when the current is further increased, but from the L-I curve, the power is not decreasing after 1.1 Jth. To prove this, the areas of integration for Fig 4.5.5 (a) were obtained from Origin Pro at J_{th}, 1.1 J_{th}, 1.2 Jth. The integrated areas are 0.218, 0.328, 0.433 respectively, meaning that the overall intensity is increasing with the increase of injection current. When the current is further increased, one can see that there is another peak at a higher energy. Therefore, the actual intensity might be still increasing but the loss in the lasers lead to the second mode, which is competitive to the main peak, and the main peak is suppressed.

In addition, as discussed above, the second peak in MR 3877 might correspond to the increase in power. However, for some devices made from MR 3881, one can also see more than one peak in the spectra, the only difference is that those peaks are very close to each other and have

similar intensity. These results reflect that narrow ridge lasers could also support multiple modes whilst a reduced number of modes would be expected, especially when the ridge is not perfect.

4.5.3 Calculation of the internal loss in the laser cavity

An important parameter in characterising lasers is the internal loss, especially in the case where the fabrication process is difficult. To determine the internal loss in the laser cavity, devices with different cavity length has been tested. However, this measurement has only been done for the devices made from MR 3877 due to limited materials.

In order to calculate the internal loss, one need to obtain the slope efficiency and external quantum efficiency from the L-I curves first. The external quantum efficiency reflects how efficient a laser can transform electrical injected energy to output light. For an ideal device, this value should be equal to 100%. For a real device, this is impossible.

Table 4.5.3 Main parameters required to calculate the internal loss

Cavity length (mm)	Slope efficiency (two facets)	External Differential Quantum efficiency (%)	Inverse of External Differential Quantum efficiency
L	$2\frac{\Delta P}{\Delta I}$	$\eta_d = 2\frac{\Delta P}{\Delta I} \times \frac{q\lambda}{hc}$	$\frac{1}{\eta_d}$
2	0.55	35.5	2.82
3	0.483	31.2	3.21
4	0.44	28.3	3.53

Table 4.5.3 shows the main parameters which will be required to calculate the internal loss in a laser cavity. In this table, L is the cavity length of a laser bar, η_d represents the external differential quantum efficiency, while q is the electric charge of a single electron, λ is the emission wavelength, h is the Planck's constant. The external differential quantum efficiency of our device is comparable with that published in papers working at similar wavelength, which equals to 0.33.[40]

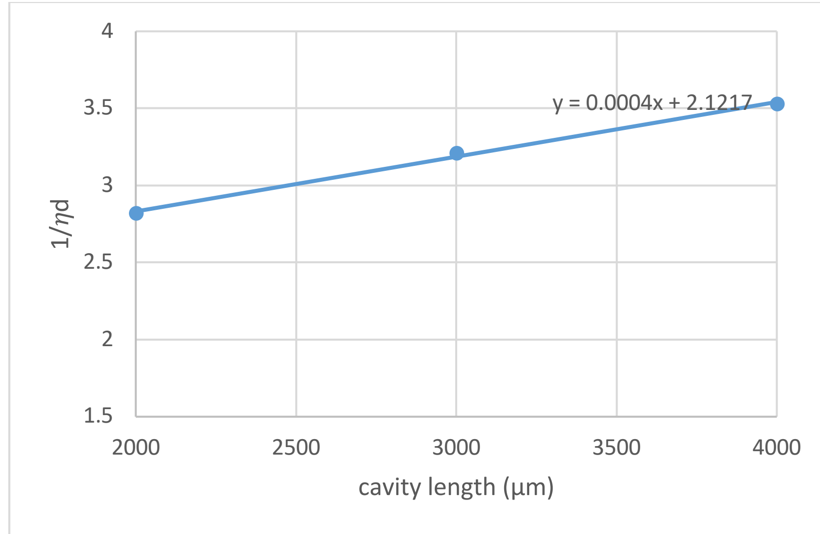

Fig 4.5.6 Relationship of cavity length and inverse external differential quantum efficiency

The dependence of cavity length on the inverse external quantum efficiency is plotted as shown in Fig 4.5.6. According to the intersection of the trend line with y-axis, one can calculate that the inverse internal quantum efficiency $\frac{1}{\eta_i} = 2.1217$, which gives $\eta_i = 47.1\%$. From this, the internal loss α_i can be calculated by the following equation, where R represents the reflectivity of the mirrors (~0.31).

$$\frac{1}{\eta_d} = \frac{1}{\eta_i}\left[1 + \frac{\alpha_i}{\ln\left(\frac{1}{R}\right)}L\right] \tag{4.5.3}$$

From this equation, the internal loss α_i is 2.2 cm^{-1}.

However, the internal efficiency and external efficiency are acceptable but not optimal. Therefore, apart from the internal loss within the laser cavity, some generated photons are reabsorbed in the cavity or transferred into other forms of energy such as heat. This parameter indicates that the structure might not be optimised.

High Reflective (HR) coated QCL

In order to test the laser in CW mode, some prepared laser bars were put into Thermal Evaporator for the HR coating which can be used to reduce operating current in the laser by reducing the mirror loss. Only back facet was coated with HR materials (MgF_2). Therefore, the light will be fully reflected back from the back facet and get out from the front facet. In this way, a reduced threshold current will then be expected. This is supported by the following equation:

$$\alpha_m = \frac{1}{2L}\ln\left(\frac{1}{R_1R_2}\right) \qquad (4.5.4)$$

Where α_m is defined as the mirror loss, which will decrease when the reflectivity is getting higher.

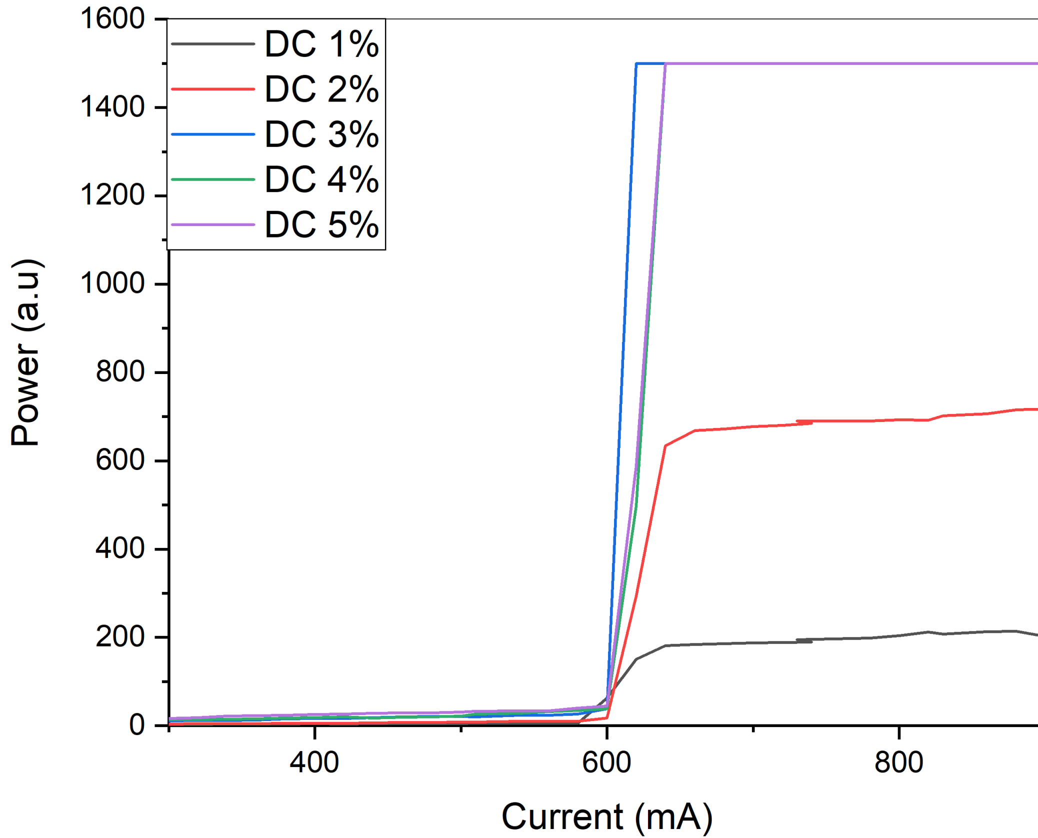

Fig 4.5.7 The L-I characteristic of the HR Coated sample

According to the L-I characteristic of an HR coated 4mm-device (MR 3877) that the threshold current is around 580 mA, which is much lower than that of an uncoated device, as expected. This could be supported by calculation, when the device is uncoated, the mirror loss can be calculated from equation (4.5.4):

Where L = 4 mm, assume $R_1 = R_2 = 0.31$

$$\alpha_{m(uncoated)} = \frac{1}{2L}\ln\left(\frac{1}{R_1R_2}\right) = 2.93\ cm^{-1}$$

$$\alpha_{total(uncoated)} = 2.2 + 2.93 = 5.13\ cm^{-1}$$

For HR coated device, L = 4 mm, Assume $R_1 = 0.31, R_2 = 1$ (fully reflected),

$$\alpha_{m(coated)} = \frac{1}{2L}\ln\left(\frac{1}{R_1R_2}\right) = 1.46\ cm^{-1}$$

$$\alpha_{total(coated)} = 2.2 + 1.46 = 3.66\ cm^{-1}$$

Therefore, the reduction in loss is:

$$\Delta\alpha_{total} = 5.13 - 3.66 = 1.47\ cm^{-1}$$

A reduced loss is obtained for the HR coated device. From the above calculation, the reduction in loss corresponds to the change in threshold current of 235 mA, the reduced threshold current is thus expected to be around 585 mA. The results shown in Fig 4.5.7 matched up with expectation.

As the HR coated sample is mounted on the copper heatsink, the heat dissipation was further improved, this is in order to test the device in CW mode. However, due to the copper heatsink was out of stock, a used copper heatsink was employed temporarily, which was imperfect to remove heat because there is leftover materials on the surface from old device. This could be a reason for why our device was not working in CW mode.

It is worth noting that the power is saturating at 1500 (a.u) when duty cycle is above 3%, which means the detector has reached the limit. However, the power is higher compared with uncoated sample, meaning that the loss is indeed reduced when covered with HR materials.

4.6 Summary and conclusion

To sum up, narrow ridge QCLs with 35 periods and 42 periods of active region have been fabricated and tested. The performance of these devices were evaluated and analysed through the experiments.

First, the current-voltage characterisation is basically consistent with the simulation, which is shown in chapter 3 that the turn on voltage is around 4~5 V and would increase with increasing periods. The IV curves from simulation and experiments also demonstrate similar trend. This means that the devices can work well from the electrical side. Secondly, according to the Power-Current curves, the laser made from MR3881 (42 periods) has a lower threshold current density than the laser made from MR3877 (35 periods), which indicates that when the period of the QCL increases, a reduced threshold current density will be obtained, due to the increase of gain. However, there would be a critical number of periods for cascade mechanism that

when the limit is reached, further increasing the number of periods will have negative effect on the device performance. For instance, large number of periods requires accumulation of more layers in the active region, which would thicken the whole structure and even increases the difficulty of growth. Therefore, some problems like quality of growth, high voltage through the structure, as well as the increase of heating might occur, this will degrade the performance of lasers. In addition, the device which is coated with HR materials has a further reduced threshold current density, meaning that the loss is decreased by reflecting the lights in the cavity. Thirdly, the spectra of these lasers demonstrate that the emission wavelength is around 5.7 µm, which is also as predicted. From our calculation, the internal loss of the laser was around 2.2 cm^{-1} and the internal efficiency is 47.1%.

Chapter 5 Conclusions and Future recommendation

In conclusion, the following problems have been addressed in my project:

(a) The effect of well thickness in the emission wavelength in an ICL has been investigated through simulation with Nextnano software. Structures from three different papers has been modelled, we were able to see that the variation of well thickness has significant effect in the emission wavelength, which means that in practical work, a small variation during MBE growth can cause a significant change in wavelength. In addition, the simulation results from Nextnano basically match with the results reported in the literature.

(b) The effect of changing well thickness in the electron distribution has also been modelled through Nextnano, and the Stark Effect was investigated by simulating a three-well structure. Hence, we were able to investigate and predict the transition in the active well, and understand how the electron distribution move as the change of electric field. From this we conclude that changing electric field will lead to the shift of electron distribution, hence the actual transition energy will be varied. This contributes to the design of tunable devices.

(c) A QCL structure designed for 5-6μm lasing has been grown in our lab and has been simulated to investigate the basic performance of this structure. The electrical performance was evaluated by observing the IV characteristic, and the Wannier-Stark energy levels were obtained to observe the transition in the active region and hence, we were able to work out the emission wavelength. The gain spectrum as a function of photon energy was also plotted to investigate the photon energy which corresponds to the maximum gain. These simulated results were also compared with our experimental work. The IV characteristics from the simulation matches with the experimental results. The emission wavelength from simulation was 6.2μm, which was 0.5μm away from the 5.7μm-predicted wavelength. As discussed above, the reason could be that the simulation tool used in my project (Nextnano) is different from the structure designer. In addition, parameters and models used in Nextnano could be slightly different with that used in designer's simulation. Apart from that, as shown in Chapter 3, 1 nm of variation in well thickness can significantly affect the emission wavelength, the emission wavelength changes from 8.8 μm to 6.8 μm.

(d) The QCL structure discussed above was also tested experimentally. From this, we were able to compare the results with simulation and explore the performance of this structure. Wafers with different number of periods were processed to investigate the effect of number of periods in reducing the threshold current density. The wafers were processed into narrow

ridge lasers with cavity length of 4mm, and the ridge width is 5μm. The device with 42 periods showed a reduced threshold current density of 2.4kA/cm^2 comparing with the device with 35 periods, which has a threshold current density of 4.1kA/cm^2. The calculation in Chapter 4 shows that the increase in periods can reflect the decrease in current density. The spectra demonstrates that the emission wavelength is about 5.7 μm, which is matched with the predicted wavelength provided by the structure designer.

Challenges and future recommendations

Overall, the simulation and experimental results meet our expectation and can help to understand the behaviour of our lasers. However, the simulation of ICL needs further improvement to at least allow the calculation of IV curves and the gain spectrum.

For the QCL, the aim of this work was to investigate the use of Nextnano software in the simulation of some key parameters in QCLs and to test these experimentally against devices grown in our laboratory. The results on emission wavelength, IV curves and threshold currents were all closely matched by experimental investigations and hence we can have confidence that the use of the Nextnano tool will be valuable for further optimization of QCLs. The CW lasing was not achieved in our HR coated sample but a reduced threshold current density was obtained. Hence, further improvements would be necessary to enable the device to work in CW mode. Regarding the power-current characteristics, it is still unclear why the power is saturated after a certain value. Therefore, this could be addressed and investigated in future experiment. Furthermore, it would be of interest to also investigate the critical number of periods.

As discussed in previous chapters that the QCL structure in this thesis is not optimal, it is thus important to optimise the structure by more simulations and experiments. The parameters should be changed to observe in which case we are able to obtain the best performance. For example, a higher doping might be applied to increase the barrier height. The well thickness could also be researched to find out a more accurate relationship with the emission wavelength. It is necessary to work out the connection between the simulation and experiments to make sure the future design can be more accurate.

In this work, QCLs emitted at 5.7 μm has been researched and well understood through the analysis with Nextnano.QCL and our experimental results. This contributes to the future optimization and design of QCLs at this wavelength. In addition, QCLs emitted at other specific wavelengths could also be studied in the future, which will lead to the investigation of incorporating our devices into real applications such as pollution monitoring, gas sensing and

medical analysis etc. In addition, enough understanding on ICL would be necessary to realise high-performance ICLs, which can replace the use of QCLs when lower operating voltage is required.

Appendix

The nextnano software works as follows. An input parameter file is required for the calculations which include the composition of materials, the thickness of each layer, temperature, doping concentration, etc.

The precise input paramters for the calculations in this thesis are presented below.

Simulation Parameters and input file for QCL:

```
  <SweepParameters>
    <SweepType>Voltage</SweepType> <!-- SweepType: "Voltage" or
"Temperature" -->
   <!-- Min, Max and delta values in mV for "Voltage", or in K for
"Temperature"-->
    <Min>20</Min>        <!-- first/min value -->
    <Max>500</Max>       <!-- last/max value -->
    <Delta>20</Delta>    <!-- increment -->
  </SweepParameters>

  <Temperature unit="K">300</Temperature> <!-- Temperature of the lattice
in Kelvin -->


  <Materials>

    <Material>
      <Name>In(x)Ga(1-x)As</Name>
      <Alloy_Composition>0.6</Alloy_Composition>
      <Alias>well</Alias>

<Effective_mass_from_kp_parameters>yes</Effective_mass_from_kp_parameters>
    </Material>

    <Material>
      <Name>Al(x)In(1-x)As</Name>
      <Alloy_Composition>0.58</Alloy_Composition>
      <Alias>barrier</Alias>

<Effective_mass_from_kp_parameters>yes</Effective_mass_from_kp_parameters>
    </Material>

    <NonParabolicity>yes</NonParabolicity>

    <UseConductionBandOffset>yes</UseConductionBandOffset>

  </Materials>


  <Superlattice>
      <Layer>
            <Material>barrier</Material>
            <Thickness unit="nm">1.9</Thickness>
      </Layer>
      <Layer>
            <Material>well</Material>
            <Thickness unit="nm">2.5</Thickness>
      </Layer>

      <Layer>
            <Material>barrier</Material>
```

```
      <Thickness unit="nm">2.0</Thickness>
</Layer>
<Layer>
      <Material>well</Material>
      <Thickness unit="nm">2.4</Thickness>
</Layer>
      <Layer>
      <Material>barrier</Material>
      <Thickness unit="nm">2.2</Thickness>
</Layer>
<Layer>
      <Material>well</Material>
      <Thickness unit="nm">2.3</Thickness>
</Layer>
      <Layer>
      <Material>barrier</Material>
      <Thickness unit="nm">2.8</Thickness>
</Layer>
<Layer>
      <Material>well</Material>
      <Thickness unit="nm">2.2</Thickness>
</Layer>
      <Layer>
      <Material>barrier</Material>
      <Thickness unit="nm">4.0</Thickness>
</Layer>
<Layer>
      <Material>well</Material>
      <Thickness unit="nm">1.3</Thickness>
</Layer>
      <Layer>
      <Material>barrier</Material>
      <Thickness unit="nm">1.3</Thickness>
</Layer>
<Layer>
      <Material>well</Material>
      <Thickness unit="nm">5.1</Thickness>
</Layer>
      <Layer>
      <Material>barrier</Material>
      <Thickness unit="nm">1.3</Thickness>
</Layer>
<Layer>
      <Material>well</Material>
      <Thickness unit="nm">4.5</Thickness>
</Layer>
      <Layer>
      <Material>barrier</Material>
      <Thickness unit="nm">1.4</Thickness>
</Layer>
<Layer>
      <Material>well</Material>
      <Thickness unit="nm">4.0</Thickness>
</Layer>
      <Layer>
      <Material>barrier</Material>
      <Thickness unit="nm">2.3</Thickness>
</Layer>

<Doping>
  <!-- homogeneous doping between starting and end point -->
```

```
        <!-- doping can be in barriers or wells or both -->
        <!-- origin = start of first barrier -->
      <DopingStart unit="nm">4.4</DopingStart>  <!-- with respect to origin
-->
      <DopingEnd unit="nm">13.3</DopingEnd>           <!-- with respect to
origin -->

    <!-- Integer in order to choose how the doping density is specified:
    ... 0 = 2D equivalent density per period in [cm^-2]
    ... 1 = 3D doping density in the doped region in [cm^-3]
    ... 2 = Averaged 3D doping density over the whole structure in [cm^-3]
-->
    <Doping_Specification>1</Doping_Specification>
    <Doping_Density>1e17</Doping_Density> <!-- Doping in units according to
Doping_Specification-->

  </Doping>

  </Superlattice>




  <Scattering>

      <Material_for_scattering_parameters>well</Material_for_scattering_par
ameters>

       <Interface_Roughness>
      <Amplitude_in_Z unit="nm">0.1</Amplitude_in_Z>
        <InterfaceAutoCorrelationType>0</InterfaceAutoCorrelationType> <!--
Correlation type: 0=Exponential, 1=Gaussian -->
      <Correlation_Length_in_XY unit="nm">8</Correlation_Length_in_XY>

      <Asymmetric_Interfaces>no</Asymmetric_Interfaces>
      <Amplitude_in_Z_Left>0.1</Amplitude_in_Z_Left>
      <Amplitude_in_Z_Right>0.2</Amplitude_in_Z_Right>

    </Interface_Roughness>

    <!-- Acoustic phonons -->
    <Acoustic_Phonon_Scattering>yes</Acoustic_Phonon_Scattering> <!--
Comment: Acoustic phonons are in general not efficient - can be neglected
in most cases -->

<AcousticPhonon_Scattering_EnergyMax>3.0</AcousticPhonon_Scattering_EnergyM
ax> <!-- Maximum acoustic phonon energy -->

        <!-- Charged impurities -->
      <!-- Effective temperature of the electrons involved in electrostatic
screeening: 3 models available -->
      <!-- model #1: Teff = T + Toffset * exp(-T/Toffset) with Toffset
specified as Temperature_Offset_parameter  -->
      <!-- model #2: self-consistent calculation (requires several
iterations of the all calculation). The ccuracy specified by
Accuracy_Self_consistent_Electron_Temperature -->
      <!-- model #3: Teff is directly specified by
Electron_Temperature_for_Screening-->
      <Model_Temperature_for_Screening>1</Model_Temperature_for_Screening>
<!-- integer 1,2 or 3 is required accordingly to the desired model -->
```

```
      <Temperature_Offset_parameter>140</Temperature_Offset_parameter> <!--
enter Toffset for model#1 only such as Teff = T + Toffset * exp(-T/Toffset)
-->

<Accuracy_Self_consistent_Electron_Temperature>0.05</Accuracy_Self_consiste
nt_Electron_Temperature>  <!-- for model #2 only: self-consistent
calculation until the effective temperature convergences below the desired
accuracy-->

<Electron_Temperature_for_Screening>200</Electron_Temperature_for_Screening
> <!-- for model#3 only: the effective temperature is directly specified -
->

      <ImpurityScattering_Strength>1.0</ImpurityScattering_Strength> <!--
1.0 is the normal physical calculation. Other values may be used for
testing the importance of impurity scattering. -->

    <Alloy_scattering>yes</Alloy_scattering>
  </Scattering>

    <Poisson>yes</Poisson>

      <Lateral_motion>
      <Material_for_lateral_motion>well</Material_for_lateral_motion>
    <!-- Lateral energy spacing  -->
    <Value unit="meV">20</Value>
  </Lateral_motion>

    <Simulation_Parameter>
      <!-- PERIODS -->
    <Coherence_length_in_Periods>1</Coherence_length_in_Periods> <!-- 1 ->
coherent transport from one period to the next | N -> coherent transport
between N+1 periods -->

      <!-- BASIS STATE CALCULATION -->
      <!-- parameters only affect the basis state calculation time. Not
critical for total calculation time. -->
      <!-- SPATIAL GRID -->
      <!--   defines number of grid points per period -->
      <Spatial_grid_spacing unit="nm">0.2</Spatial_grid_spacing>
      <!-- number of periods used for basis state calculation only: -->
      <!--   corresponds to 2N+1 k points per miniband -->
      <Number_of_lateral_periods_for_band_structure>2</Number_of_lateral_pe
riods_for_band_structure>
      <!-- number of grid points/period * (2N+1) should stay below ~10^4
for fast calculation time -->



      <!-- ENERGY GRID -->
      <!-- critical for calculation time! -->
      <!-- It holds for higher temperatures: More broadening, i.e. less
energy grid points are sufficient. -->
    <Energy_grid_spacing unit="meV">5</Energy_grid_spacing>  <!--
homogeneously spaced grid -->

    <Emin_shift unit="meV">0</Emin_shift> <!-- 0 is the default value - a
negative value increases the energy range of the Green functions towards
low energies -->
    <Emax_shift unit="meV">0</Emax_shift>  <!--  0 is the default value - a
positive value increases the energy range of the Green functions towards
```

```
high energies -->

    <Energy_Range_Lateral unit="meV">300</Energy_Range_Lateral> <!-- xy-
direction, evaluated from lowest state -->
    <Energy_Range_Axial unit="meV">500</Energy_Range_Axial> <!-- z-
direction,  evaluated from lowest state/miniband -->

    <!-- The self-consistent loop ends successfully if the 2 following
convergence factors are reached for the lesser Green's function and the
current (relative difference between two consecutive iterations) -->
    <Convergence_Value_GF>1e-3</Convergence_Value_GF>
    <Convergence_Value_Current>1e-3</Convergence_Value_Current>

    <!-- Number of maximum iterations if the above convergence values are
not reached -->
    <!-- Higher values give more accurate results. -->
    <N_max_iterations>200</N_max_iterations>

  </Simulation_Parameter>

  <Output>
    <!-- In order to output 2D energy resolved graphs-->
    <EnergyResolvedPlots>yes</EnergyResolvedPlots>

<EnergyResolvedPlots_MinimumEnergyGridSpacing>2.0</EnergyResolvedPlots_Mini
mumEnergyGridSpacing>

    <!-- Energy resolved gain for a specified photon energy-->
    <EnergyResolved_Gain>yes</EnergyResolved_Gain>
  </Output>

  <Gain>
      <!-- GainMethod:
               -1 .. no gain calculation
                  0 .. gain without self-consistency only
                  1 .. gain with self-consistency only
                  2 .. gain with and without self-consistency
      -->
    <GainMethod>0</GainMethod>

      <!-- without self-consistency: -->
  <dE_Phot unit="meV">5</dE_Phot> <!-- energy spacing between two photon
energies -->
      <Ephoton_Min unit="meV">100</Ephoton_Min>
  <Ephoton_Max unit="meV">200</Ephoton_Max>

      <!-- with self-consistency: -->
    <dE_Phot_Self_Consistent unit="meV">5</dE_Phot_Self_Consistent> <!--
energy spacing between two photon energies -->
    <Ephoton_Min_Self_Consistent
unit="meV">100</Ephoton_Min_Self_Consistent>
    <Ephoton_Max_Self_Consistent
unit="meV">200</Ephoton_Max_Self_Consistent>


<MaxNumber_SelfConsistent_Iterations>10</MaxNumber_SelfConsistent_Iteration
s>
    <ConvergenceFactor_Gain_SelfConsistent>1e-
3</ConvergenceFactor_Gain_SelfConsistent>

    <!-- Calculation of gain only between the following values of potential
```

```
drop per period -->
    <Vmin unit="mV">160</Vmin>
    <Vmax unit="mV">400</Vmax>

  </Gain>


</nextnano.QCL>
```

References

[1] M. S. Vitiello, G. Scalari, B. Williams, and P. De Natale, "Quantum cascade lasers: 20 years of challenges," *Optics Express,* vol. 23, pp. 5167-5182, 2015/02/23 2015.

[2] R. F. K. a. R. A. Suris, "Possibility of the Amplification of Electromagnetic Waves in a Semiconductor with a Superlattice1971," *Soviet Physics—Semiconductors,* vol. 5, 1971.

[3] A. Y. Cho Molecule Beam Epitaxy, (Woodbury, NY: AIP Press) 1997.

[4] https://www.rp-photonics.com/population_inversion.html

[5] S.M.SZE and KWOK K. NG. Physics of semiconductor devices, (Wiley Interscience) 2007

[6] J. Faist, F. Capasso, D. L. Sivco, C. Sirtori, A. L. Hutchinson, and A. Y. Cho, "Quantum cascade laser," Science 264(5158), 553-556 1994.

[7] Y. Yao, A. J. Hoffman, and C. F. Gmachl, "Mid-infrared quantum cascade lasers," Nat. Photonics 6(7), 432-439 2012.

[8] Y. Bai, S. Slivken, S. Kuboya, S. R. Darvish, and M. Razeghi, "Quantum cascade lasers that emit more light than heat," *Nat Photon,* vol. 4, pp. 99-102, 02//print 2010.

[9] P. Q. Liu, A. J. Hoffman, M. D. Escarra, K. J. Franz, J. B. Khurgin, Y. Dikmelik*, et al.*, "Highly power-efficient quantum cascade lasers," *Nat Photon,* vol. 4, pp. 95-98, 02//print 2010.

[10] Y. Bai, N. Bandyopadhyay, S. Tsao, S. Slivken, and M. Razeghi, "Room temperature quantum cascade lasers with 27% wall plug efficiency," *Applied Physics Letters,* vol. 98, p. 181102, 2011.

[11] M. Beck, D. Hofstetter, T. Aellen, J. Faist, U. Oesterle, M. Ilegems*, et al.*, "Continuous Wave Operation of a Mid-Infrared Semiconductor Laser at Room Temperature," *Science,* vol. 295, p. 301, 2002.

[12] Y. Bai, N. Bandyopadhyay, S. Tsao, E. Selcuk, S. Slivken, and M. Razeghi, "Highly temperature insensitive quantum cascade lasers," *Applied Physics Letters,* vol. 97, p. 251104, 2010.

[13] J. Devenson, "InAs/AlSb short wavelength quantum cascade lasers," 2010.

[14] I. Vurgaftman, R. Weih, M. Kamp, J. R. Meyer, C. L. Canedy, C. S. Kim*, et al.*, "Interband cascade lasers," *Journal of Physics D: Applied Physics,* vol. 48, p. 123001, 2015.

[15] L. Li, H. Ye, Y. Jiang, R. Q. Yang, J. C. Keay, T. D. Mishima*, et al.*, "MBE-grown long-wavelength interband cascade lasers on InAs substrates," *Journal of Crystal Growth,* vol. 425, pp. 369-372, 9/1/ 2015.

[16] R. Q. Yang, "Infrared laser based on intersubband transitions in quantum wells," *Superlattices and Microstructures,* vol. 17, pp. 77-83, 1995/01/01/ 1995.

[17] I. Vurgaftman, J. R. Meyer, and L. R. Ram-Mohan, "Mid-IR vertical-cavity surface-emitting lasers," *IEEE Journal of Quantum Electronics,* vol. 34, pp. 147-156, 1998.

[18] I. Vurgaftman, W. W. Bewley, C. L. Canedy, C. S. Kim, M. Kim, J. R. Lindle*, et al.*, "Mid-IR Type-II Interband Cascade Lasers," *IEEE Journal of Selected Topics in Quantum Electronics,* vol. 17, pp. 1435-1444, 2011.

[19] I. Vurgaftman, W. W. Bewley, C. L. Canedy, C. S. Kim, M. Kim, C. D. Merritt*, et al.*, "Rebalancing of internally generated carriers for mid-infrared interband cascade lasers with very low power consumption," *Nature Communications,* vol. 2, p. 7, Dec 2011.

[20] M. Dallner, S. Hofling, and M. Kamp, "Room-temperature operation of InAs-based interband-cascade-lasers beyond 6 μm," *Electronics Letters,* vol. 49, pp. 286-287, 2013.

[21] Z. Tian, L. Li, H. Ye, R. Q. Yang, T. D. Mishima, M. B. Santos*, et al.*, "InAs-based interband cascade lasers with emission wavelength at 10.4 μm," *Electronics Letters,* vol. 48, pp. 113-114, 2012.

[22] Z. Tian, Y. Jiang, L. Li, R. T. Hinkey, Z. W. Yin, R. Q. Yang*, et al.*, "InAs-Based Mid-Infrared Interband Cascade Lasers Near 5.3 μm," *Ieee Journal of Quantum Electronics,* vol. 48, pp. 915-921, Jul 2012.

[23] C. L. Canedy, W. W. Bewley, J. R. Lindle, J. A. Nolde, D. C. Larrabee, C. S. Kim*, et al.*, "Interband Cascade Lasers with Wavelengths Spanning 2.9 μm to 5.2 μm," *Journal of Electronic Materials,* vol. 37, pp. 1780-1785, 2008/12/01 2008.

[24] C. J. Hill and R. Q. Yang, "MBE growth optimization of Sb-based interband cascade lasers," *Journal of Crystal Growth,* vol. 278, pp. 167-172, 2005/05/01/ 2005.
[25] R. Q. Yang, J. D. Bruno, J. L. Bradshaw, J. T. Pham, and D. E. Wortman, "Interband cascade lasers: progress and challenges," *Physica E: Low-dimensional Systems and Nanostructures,* vol. 7, pp. 69-75, 2000/04/01/ 2000.
[26] Y. C. Jiang, L. Li, H. Ye, R. Q. Yang, T. D. Mishima, M. B. Santos*, et al.*, "InAs-Based Single-Mode Distributed Feedback Interband Cascade Lasers," *Ieee Journal of Quantum Electronics,* vol. 51, Sep 2015.
[27] C. J. Chang-Hasnain, E. Kapon, and R. Bhat, "Spatial mode structure of broad-area semiconductor quantum well lasers," *Applied Physics Letters,* vol. 54, pp. 205-207, 1989/01/16 1989.
[28] M. Kanskar, Y. He, J. Cai, C. Galstad, S. H. Macomber, E. Stiers*, et al.*, "53% wallplug efficiency 975nm distributed feedback broad area laser," *Electronics Letters,* vol. 42, pp. 1455-1457, 2006.
[29] C. M. Schultz, P. Crump, H. Wenzel, O. Brox, F. Bugge, and G. Erbert, "Narrow Vertical Far-Field 975-nm Broad-Area DFB Lasers for Wide Temperature Range Operation," *IEEE Photonics Technology Letters,* vol. 21, pp. 593-595, 2009.
[30] W. Bewley, L. Canedy, C .S. Kim, M. Kim, J. R. Lindle, J. Abell, *et al.,* "Ridge-width dependence of midinfrared interband cascade laser characteristics," *Optical Enigneering* vol.49 p. 111116, 2010.
[31] C. S. Kim, M. Kim, W. W. Bewley, J. R. Lindle, C. L. Canedy, J. Abell*, et al.*, "Corrugated-sidewall interband cascade lasers with single-mode midwave-infrared emission at room temperature," *Applied Physics Letters,* vol. 95, p. 231103, 2009/12/07 2009.
[32] L. Li, L. Zhao, Y. Jiang, R. Q. Yang, J. C. Keay, T. D. Mishima*, et al.*, "Single-waveguide dual-wavelength interband cascade lasers," *Applied Physics Letters,* vol. 101, p. 171118, 2012.
[33] Y. C. Jiang, L. Li, Z. B. Tian, H. Ye, L. H. Zhao, R. Q. Yang*, et al.*, "Electrically widely tunable interband cascade lasers," *Journal of Applied Physics,* vol. 115, p. 17, Mar 2014.
[34] S. Suchalkin, M. V. Kisin, S. Luryi, G. Belenky, F. J. Towner, J. D. Bruno*, et al.*, "Widely tunable type-II interband cascade laser," *Applied Physics Letters,* vol. 88, p. 031103, 2006/01/16 2006.
[35] R. Q. Yang, C.-H. Lin, S. J. Murry, S. S. Pei, H. C. Liu, M. Buchanan*, et al.*, "Interband cascade light emitting diodes in the 5–8 µm spectrum region," *Applied Physics Letters,* vol. 70, pp. 2013-2015, 1997/04/14 1997.
[36] W. L. Bloss, "Electric field dependence of the eigenstates of coupled quantum wells," *Journal of Applied Physics,* vol. 67, pp. 1421-1424, 1990/02/01 1990.
[37] P. F. Yuh and K. L. Wang, "Large Stark effects for transitions from local states to global states in quantum well structures," *IEEE Journal of Quantum Electronics,* vol. 25, pp. 1671-1676, 1989.
[38] J. Scheuermann, R. Weih, M. von Edlinger, L. Nähle, M. Fischer, J. Koeth*, et al.*, "Single-mode interband cascade lasers emitting below 2.8 µm," *Applied Physics Letters,* vol. 106, p. 161103, 2015/04/20 2015.
[39] L. Li, Y. Jiang, H. Ye, R. Q. Yang, T. D. Mishima, M. B. Santos*, et al.*, "Low-threshold InAs-based interband cascade lasers operating at high temperatures," *Applied Physics Letters,* vol. 106, p. 251102, 2015/06/22 2015.
[40] A.Christou, C. C.Zhang M. Linick*,* " Tunable wavelength surface quantum cascade lasers for chemical sensors in the 3-6 um spectral region,"*Proceedings of SPIE,* 2007/10/16 2007.